A two-dimensional spectral-element method for computing spherical-earth seismograms – I. Moment-tensor source

Tarje Nissen-Meyer, Alexandre Fournier, F.A. Dahlen

Geophys. J. Int. (2007) **168,** 1067–1092 doi: 10.1111/j.1365-246X.2006.03121.x

A two-dimensional spectral-element method for computing spherical-earth seismograms – I. Moment-tensor source

Tarje Nissen-Meyer,[1] Alexandre Fournier[2] and F. A. Dahlen[1]

[1]*Department of Geosciences, Princeton University, Princeton,* NJ 08544, *USA. E-mail: tarje@princeton.edu*
[2]*Laboratoire de Géophysique Interne et Tectonophysique, Université Joseph Fourier,* 38041 *Grenoble Cedex* 9, *France*

Accepted 2006 June 29. Received 2006 May 11; in original form 2005 November 16

SUMMARY

We develop a spectral-element method for computing the full 3-D moment-tensor and point-force response of a spherically symmetric earth model in a 2-D semi-circular computational domain. The full elastodynamic response to a six-component moment tensor at an earthquake hypocentre and a three-component point force at a seismic station can be determined by solving six independent 2-D problems, three for a monopole source, two for a dipole source, and one for a quadrupole source. This divide-and-conquer 3-D to 2-D reduction strategy provides a basis for the efficient computation of exact Fréchet sensitivity kernels in a spherically symmetric earth, with all wavefield features accounted for. To focus on the novel inclusion of the full source in a cylindrical coordinate system, we describe the 2-D weak formulation of the set of elastodynamic equations, its discretization using spectral elements, and the associated axial boundary conditions and source representations for each of the excitation types in the case of a homogeneous, solid elastic sphere. The method is numerically validated against both analytical solutions and normal-mode summation.

Key words: elastic-wave theory, finite-element methods, global seismology, numerical techniques, seismic-wave propagation, synthetic seismograms.

1 INTRODUCTION

The sensitivity of seismic waves to 3-D earth structure is becoming increasingly well understood and important in the age of high-quality digital broadband seismic data, improved path coverage, and computational advances in both hardware and software. Our aim is to construct full waveform sensitivity kernels in the first-order Born approximation as suggested in the preceding paper (Nissen-Meyer *et al.* 2007), allowing for diffracted-phase traveltime inversions to better sample regions like D″. To do this, one needs to know the velocity and strain responses to all six source moment-tensor components and three station single-force polarizations in a spherically symmetric reference model throughout space and time, while reaching wavelengths that correspond to the structures of interest. Further constraints imposed on the calculation of these responses are the ease of parallelization to reach sufficient frequencies on conventional clusters and high accuracy for the entire wavefield at any spatial and temporal distance from the source.

The problem of generating spherical-earth synthetics has been attacked from many different angles. Spherical harmonics are utilized for normal-mode summation (Dahlen & Tromp 1998; Lognonné & Romanowicz 1990) or numerical computation of the Green function in the frequency domain (GEMINI, Friederich & Dalkolmo 1995). Both approaches account for the moment tensor and complete waveforms, however, mode summation is computationally problematic when calculating complete, high-frequency seismograms (e.g. Geller & Ohminato 1994). GEMINI overcomes the problem of intense summation by numerically integrating the elastodynamic system of ordinary differential equations in the frequency domain. The computational effort here is proportional to the length and number of seismograms, which for our postulated storage of long time series at all spatial points is again a formidable challenge. A technique based on weighted residuals is the direct solution method or DSM (Geller & Ohminato 1994; Cummins *et al.* 1994a,b), a Galerkin formulation expanding the solution to the frequency-domain elastodynamic weak form in terms of trial functions, which has recently been extended to transversely isotropic media up to frequencies of 2 Hz (Kawai *et al.* 2006). This method is highly efficient in computing single, complete seismograms at a range of frequencies, but the cost mainly depends on the number of frequencies and trial functions, number and length of seismograms due to the inverse Fourier transform performed to obtain time-series. DSM computation times seem intractable for our purposes of storing the entire wavefield since the collection of Green tensors appropriate for inversions requires many long time-series sampling a large number of frequencies. Furthermore, for all of the above methods, current implementations do not simultaneously calculate the velocity field and strain tensor (the DSM uses piecewise radial splines for displacements), which may be a major challenge since both the spatial and temporal derivatives can cause significant extra

CPU time and degraded accuracy. Additionally, the global expansion, for example, in terms of spherical harmonics, severely limits distributed computing in a parallel sense, which is problematic since the storage of all waveforms exceeds any reasonable hardware device capabilities on a single machine. While theoretically expedient for our purposes, most of the actual implementations of the methods outlined above are either not stable or seem computationally unfeasible for storing global waveforms up to 1 Hz signals. Hence, our modus operandi will be a direct, time-domain, and easily parallelizable numerical representation of the elastic wave equation, evaluating the velocity and strain tensor as natural field variables at grid points throughout the domain.

A plethora of such grid-based numerical approaches to elastodynamics for 2-D and 3-D has emerged in the last few decades, ranging from purely local operators to global functional representation. Axisymmetric finite difference (FD) methods (Chaljub & Tarantola 1997; Igel & Weber 1995, 1996; Thomas *et al.* 2000; Toyokuni *et al.* 2005) make use of the lateral model invariance and solve the 3-D wave propagation problem on a 2-D mesh. Being based on the strong form of the equations of motion, these algorithms are unfortunately not capable of including the full moment tensor and all three single-force sources. In the typical velocity–stress formulation, it is also not possible to simultaneously compute the displacement, velocity and strain tensor without introducing additional expensive and accuracy-degrading derivative operations. Furthermore, FD methods generally suffer from large numerical dispersion, especially for surface waves due to approximate free-surface boundary conditions and diffracted waves near internal discontinuities due to the staggered grid (Robertsson 1996). This is a crucial drawback inasmuch as one of our primary interests is the computation of sensitivity kernels around the D″ region. The accuracy of such local FD operators has been subject to improvements which lead to optimal operators minimizing the joint error in spatial and temporal discretization (Geller & Takeuchi 1998; Takeuchi *et al.* 2000), but efficient meshing of the globe remains an unsurmounted task. Pseudospectral solutions for global, axisymmetric domains (e.g. Furumura *et al.* 1998), while known to be more accurate in general, are inferior to FD when sharp discontinuities are included and face issues of parallelization due to the global memory access required by the Fourier transform (Mizutani *et al.* 2000). Classical finite elements (e.g. Bao *et al.* 1998) which are naturally adaptable to any geometry, have been applied to seismic-wave propagation, but remain largely inefficient due to significant numerical dispersion and expensive time marching as a result of inverting large linear systems. Most recently, the arbitrary high-order discontinuous Galerkin method has successfully been implemented for 2-D global wave propagation (Käser & Dumbser 2006). While this approach looks promising with respect to accuracy and efficiently meshing the globe, it is still in its seismological infancy and will be subject to benchmarking both accuracy and computational cost.

The most prevalent method that has been developed to the point of tackling full complex 3-D wave propagation in detail is the spectral-element method (SEM) on regional (Faccioli *et al.* 1997; Seriani 1998; Komatitsch & Vilotte 1998; Komatitsch & Tromp 1999) and especially global scales (Komatitsch & Tromp 2002a,b; Komatitsch *et al.* 2003; Chaljub *et al.* 2003; Chaljub & Valette 2004; Chaljub *et al.* 2006). However, the SEM has globally been applied to minimal periods of 3.5 s (Tsuboi *et al.* 2003) due to computational limitations even on the largest existing machines. For our purposes of calculating seismic sensitivity, the amount of potential data storage in 3-D exceeds any reasonable hardware capabilities as we need to store spatial grid points every few kilometres to resolve frequencies up to one hertz, that is, the maximal frequencies in global seismology. Hence, we seek an alternative in solving the 3-D problem with a computational effort corresponding to 2-D much like axisymmetric FD. In the preceding paper (Nissen-Meyer *et al.* 2007), we derive a weak formulation for 3-D wave propagation through spherically symmetric background models in a 2-D domain. For a given earthquake location, the problem at hand is a number of 2-D weak equations to be solved numerically with the remaining angular dependence then known via analytical continuation. Based on our criteria to compute sensitivity kernels (accurate wavefields for all distances and phases, high frequencies, full moment tensor), we note that no existing approach meets these constraints and we, therefore, devise an axisymmetric approach based on the spectral-element technique (e.g. Bernardi *et al.* 1999; Fournier *et al.* 2004) which can reach desirable resolutions on conventional Beowulf clusters and can handle the full source representation.

This paper is organized as follows: In Section 2, we briefly recall, summarize and recast the 2-D weak formulation of the elastodynamic equations derived in the previous paper (Nissen-Meyer *et al.* 2007), restricting attention to an everywhere solid earth model in the interest of simplicity. In Section 3, we specify the crucial concepts of the spectral-element method in an axisymmetric setting to compose the toolbox needed to discretize the system with a specific focus on discretization at the axis. In Section 4, we synthesize elemental contributions to a global system and associated evolution in time, and then successively depict the discretized versions of source, mass, and stiffness terms. Section 5 validates the implementation against both analytical and normal-mode reference solutions. Finally, there are extensive appendices dealing with definitions of mapping relations and polynomial representations (Appendix A), the full discretized and optimized stiffness system for all source types (Appendix B), and a derivation of toroidal eigenfunctions in a homogeneous sphere (Appendix C), which constitute the reference solution needed in Section 5.1. The problems of discretizing the fluid core, solid-fluid coupling, more reasonable 1-D background models and mesh optimization thereof at high frequencies as well as parallelization will be addressed in a subsequent paper.

2 EQUATIONS OF MOTION: SOLID MEDIA

As a first step toward the long-term goal of computing full spherical-earth Fréchet sensitivity kernels numerically, we set out to solve the 3-D elastodynamic equations of motion in a solid, isotropic, non-rotating, non-gravitating earth model $\oplus$. In the variational or weak formulation, one seeks a solution **u** in a space of admissible displacements having square-integrable derivatives, such that for all admissible test functions (also known as trial solutions or virtual displacements, see Hughes (1987)) **w**,

$$\int_{\oplus} \left\{ \rho(\mathbf{r})\mathbf{w}(\mathbf{r}) \cdot \partial_t^2 \mathbf{u}(\mathbf{r},t) + \lambda(\mathbf{r})\left[\nabla \cdot \mathbf{w}(\mathbf{r})\right]\left[\nabla \cdot \mathbf{u}(\mathbf{r},t)\right] + \mu(\mathbf{r})\nabla\mathbf{w}(\mathbf{r}) : \left[\nabla\mathbf{u}(\mathbf{r},t) + (\nabla\mathbf{u}(\mathbf{r},t))^{\mathrm{T}}\right] \right\} d^3\mathbf{r}$$
$$= \begin{Bmatrix} \hat{\mathbf{p}} \cdot \mathbf{w}(r_{\mathrm{r}}\hat{\mathbf{z}})\,\delta(t) \\ \mathbf{M} : \nabla\mathbf{w}(r_{\mathrm{s}}\hat{\mathbf{z}})\,H(t) \end{Bmatrix}, \tag{1}$$

where ρ is the mass density, λ and μ the Lamé parameters, $\hat{\mathbf{p}}$ the single-force unity vector at the receiver at radius r_{r}, and $\mathbf{M}$ the moment tensor at the source at radius r_{s}, assuming that source and receiver locations have been rotated to the pole as detailed in Nissen-Meyer *et al.* (2007). As usual, $\delta(t)$ and $H(t)$ are the Dirac impulse and Heaviside step functions, respectively characterizing the temporal evolution of the point-force and moment-tensor sources. Restricting ourselves to spherically symmetric earth models such that $\lambda = \lambda(r)$, $\mu = \mu(r)$, $\rho = \rho(r)$, we may revert to a 2-D computational domain (Nissen-Meyer *et al.* 2007). While retaining the (s, ϕ, z) cylindrical coordinate system for the monopole and quadrupole cases, we develop the dipole system in the $(+, -, z)$ system, such that

$$u_{\pm}(s,z) = \tfrac{1}{2}[u_s(s,z) \pm u_\phi(s,z)], \tag{2}$$

$$w_{\pm}(s,z) = \tfrac{1}{2}[w_s(s,z) \pm w_\phi(s,z)], \tag{3}$$

inasmuch as this enables easier implementation of the axial boundary conditions given by

$$\begin{aligned} &\text{Monopole:} && (u_s = w_s)_{s=0} = 0, \\ &\text{Dipole:} && (u_- = w_- = u_z = w_z)_{s=0} = 0, \\ &\text{Quadrupole:} && (u_s = w_s = u_\phi = w_\phi = u_z = w_z)_{s=0} = 0. \end{aligned} \tag{4}$$

Following Nissen-Meyer *et al.* (2007), eqs (56), (63), and (71), we write the system, equivalent to eq. (1), in a 2-D semi-circular computational domain Ω for monopole, dipole and quadrupole sources, respectively, as

$$\int_\Omega \left\{ \rho\left(w_s\partial_t^2 u_s + w_z\partial_t^2 u_z\right) + \lambda\left(\partial_s w_s + \partial_z w_z + s^{-1}w_s\right)\left(\partial_s u_s + \partial_z u_z + s^{-1}u_s\right) \right.$$
$$\left. + 2\mu\left(\partial_s w_s \partial_s u_s + \partial_z w_z \partial_z u_z + s^{-2} w_s u_s\right) + \mu(\partial_s w_z + \partial_z w_s)(\partial_s u_z + \partial_z u_s) \right\} s\, ds\, dz$$
$$= \frac{1}{2\pi} \begin{Bmatrix} p_z\, w_z(0, r_{\mathrm{r}})\,\delta(t) \\ M_{zz}\,\partial_z w_z(0, r_{\mathrm{s}})\,H(t) \\ \frac{1}{2}\left(M_{xx} + M_{yy}\right)\left[2\partial_s w_s(0, r_{\mathrm{s}})\right] H(t) \end{Bmatrix}, \tag{5}$$

$$\int_\Omega \left\{ \rho\left(2w_+\partial_t^2 u_+ + 2w_-\partial_t^2 u_- + w_z\partial_t^2 u_z\right) + \lambda\left(\partial_s w_+ + \partial_s w_- + \partial_z w_z + 2s^{-1}w_-\right)\left(\partial_s u_+ + \partial_s u_- + \partial_z u_z + 2s^{-1}u_-\right) \right.$$
$$+ 2\mu[(\partial_s w_+ + \partial_s w_-)(\partial_s u_+ + \partial_s u_-) + \partial_z w_z \partial_z u_z + 4s^{-2} w_- u_-] + \mu(\partial_s w_z + \partial_z w_+ + \partial_z w_-)(\partial_s u_z + \partial_z u_+ + \partial_z u_-)$$
$$\left. + \mu\left(\partial_s w_+ - \partial_s w_- + 2s^{-1}w_-\right)\left(\partial_s u_+ - \partial_s u_- + 2s^{-1}u_-\right) + \mu\left(\partial_z w_+ - \partial_z w_- + s^{-1}w_z\right)\left(\partial_z u_+ - \partial_z u_- + s^{-1}u_z\right) \right\} s\, ds\, dz$$
$$= \frac{1}{\pi} \begin{Bmatrix} (p_x \text{ or } p_y)\, w_+(0, r_{\mathrm{r}})\,\delta(t) \\ (M_{xz} \text{ or } M_{yz})\left[\partial_s w_z(0, r_{\mathrm{s}}) + \partial_z w_+(0, r_{\mathrm{s}})\right] H(t) \end{Bmatrix}, \tag{6}$$

$$\int_\Omega \left\{ \rho(w_s\partial_t^2 u_s + w_z\partial_t^2 u_z + w_\phi\partial_t^2 u_\phi) + \lambda\left[\partial_s w_s + \partial_z w_z + s^{-1}(w_s - 2w_\phi)\right]\left[\partial_s u_s + \partial_z u_z + s^{-1}(u_s - 2u_\phi)\right] \right.$$
$$+ 2\mu\left[\partial_s w_s \partial_s u_s + \partial_z w_z \partial_z u_z + s^{-2}(w_s - 2w_\phi)(u_s - 2u_\phi)\right] + \mu(\partial_s w_z + \partial_z w_s)(\partial_s u_z + \partial_z u_s)$$
$$\left. + \mu\left[\partial_s w_\phi + s^{-1}(2w_s - w_\phi)\right]\left[\partial_s u_\phi + s^{-1}(2u_s - u_\phi)\right] + \mu(\partial_z w_\phi + 2s^{-1}w_z)\left(\partial_z u_\phi + 2s^{-1}u_z\right) \right\} s\, ds\, dz$$
$$= \frac{1}{\pi}\left[\tfrac{1}{2}(M_{xx} - M_{yy}) \text{ or } M_{xy}\right]\left[2\partial_s w_+(0, r_{\mathrm{s}})\right] H(t). \tag{7}$$

In the following two sections, we introduce a spectral-element approach to solve the above systems. This step from the analytical weak form to its numerical counterpart encompasses the restriction from an infinite-dimensional space to a finite-dimensional space of solutions in the context of a Galerkin method (Hughes 1987).

3 AXISYMMETRIC SPECTRAL-ELEMENT METHODOLOGY

In this section, we give a brief overview of the aspects of the spectral-element method (SEM) that are relevant for the discretization, which we take up in the following sections. The reader is referred to the detailed literature for a full description of the approach, for example, Deville *et al.* (2002) and Karniadakis & Sherwin (1999) on the mathematical foundations of the SEM with a focus on fluid dynamics; Komatitsch & Vilotte (1998), Komatitsch & Tromp (1999, 2002a), Chaljub *et al.* (2003) and Chaljub *et al.* (2006) on the elastodynamic SEM; and Bernardi *et al.* (1999) and Fournier *et al.* (2004) on discretizing an axisymmetric system.

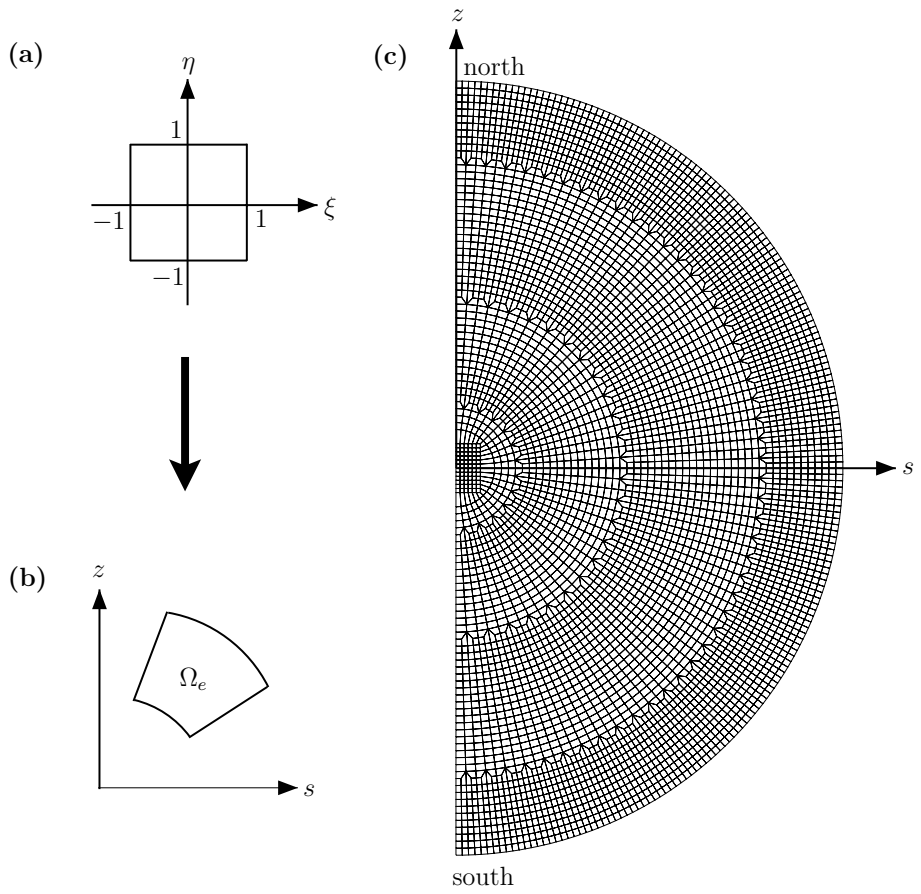

Figure 1. The mesh architecture. The geometric mapping mentioned in Section 3.1 transforms the unit square element (a), within which all computations are undertaken, into any quadrilateral element Ω_e or $\bar{\Omega}_e$ (b). (c) shows the actual mesh used in the simulations described in Section 5. Three different element geometries, as defined in Appendix A1 and Fig. A1, are used to construct this mesh such that spacing variations are kept small. The radius of the earth is r_0, and the left straight edge is the non-physical axis of symmetry for which we employ different discretization rules due to the appearance of singularities.

3.1 Geometrical mapping and discretization

As in any element-based method, we discretize and decompose the continuous, open domain Ω with boundary $\partial\Omega$ into a union of non-overlapping elements. For clarity, we shall distinguish the so-called axial elements, which share an edge with the axis of symmetry $s = 0$, from the remaining ones. Any axial element is then denoted by $\bar{\Omega}_e$, $e = 1, \ldots, \bar{n}$, while a non-axial element is represented by Ω_e, $e = 1, \ldots, n$, such that the total number of elements forming the skeleton of the spectral-element mesh is $n + \bar{n}$. Throughout the paper, we will consistently utilize an overbar to identify axial quantities. This decomposition permits us to break any global integration over Ω up into $n + \bar{n}$ local integrations, each spanning their respective elements, such that we define all integrands on the elemental level and only connect these to the global system when marching forward in time, as detailed in Section 4. In the 2-D spectral-element discretization used here, we confine Ω_e or $\bar{\Omega}_e$ to be a quadrilateral image of a reference square spanning $-1 \leq \xi \leq 1$, $-1 \leq \eta \leq 1$, defined by the invertible mapping $s = s(\xi, \eta)$, $z = z(\xi, \eta)$ (Figs 1a and b). The exclusion of other geometries such as triangular elements will not hamper the feasibility of our approach given the spherical nature of spherical-earth discontinuities, that is, the mildly deformed elemental shape. The D-shaped, planar domain with radius r_0 is shown in Fig. 1(c), along with the mesh discretization as used throughout this paper. Note that we included several conforming coarsening levels to reduce grid spacing variations (Komatitsch & Tromp 2002a) which generally trade off the time step (depending on the minimal spacing) with the frequency resolution (depending on the maximal spacing) in any numerical scheme. The centre is discretized using rectangular elements (Chaljub 2000). The expression of the mapping depends on the elemental shape and is either analytical or subparametric (Fournier *et al.* 2004). Explicit formulae and illustrations are given in Appendix A1. With a given element shape, we can then compute the elemental Jacobian

$$\mathcal{J}(\xi, \eta) = \frac{\partial(s, z)}{\partial(\xi, \eta)} = \det \begin{pmatrix} \partial_\xi s & \partial_\eta s \\ \partial_\xi z & \partial_\eta z \end{pmatrix}. \tag{8}$$

Derivatives ∂_s and ∂_z of a function $u(s(\xi, \eta), z(\xi, \eta))$ map into the reference square as

$$\partial_s u(s, z) = \left[\partial_\eta z(\xi, \eta)\partial_\xi u(s(\xi, \eta), z(\xi, \eta)) - \partial_\xi z(\xi, \eta)\partial_\eta u(s(\xi, \eta), z(\xi, \eta))\right] \mathcal{J}^{-1}(\xi, \eta), \tag{9}$$

$$\partial_z u(s,z) = [-\partial_\eta s(\xi,\eta)\partial_\xi u(s(\xi,\eta),z(\xi,\eta)) + \partial_\xi s(\xi,\eta)\partial_\eta u(s(\xi,\eta),z(\xi,\eta))]\mathcal{J}^{-1}(\xi,\eta). \tag{10}$$

Elements $\bar{\Omega}_e$ adjacent to the non-physical boundary $s = 0$ (i.e. the axis of symmetry) are treated separately to accommodate singularities arising from terms involving s^{-1} in the equations of motion (5)–(7). We describe the treatment of the non-axial elements in Section 3.2 and briefly discuss the additional complexities for the axial elements in Section 3.3.

3.2 General non-axial functional discretization

The spectral-element approach presented here relies on quadrature of the Gauss–Lobatto type, allowing us to enforce continuity across element boundaries conveniently by including the nodes $\xi = -1, 1$. Nth-order Legendre polynomials P_N (see Appendix A, eq. A15) are then invoked to define the most accurate and natural quadrature rule (Deville *et al.* 2002). Quadrature nodes are hereupon defined as the zeroes of $(1-\xi^2)\partial_\xi P_N(\xi)$, denoted as Gauss–Lobatto–Legendre (GLL) points $\xi_p, 0 \le p \le N$. To interpolate functions upon these GLL nodes, we introduce Lagrange interpolating functions $l_i^N(\xi_p)$ of polynomial order N, $0 \le i,\ p \le N$, such that: $l_i^N(\xi_p) = \delta_{ip}$ (see Appendix A2). For clarity, we shall denote GLL nodes in the ξ direction as ξ_i and in the η direction as η_j. The choice of Lagrangian interpolation upon GLL nodes yields the desirable property of a diagonal mass matrix, thereby greatly reducing the effort on time marching (see Section 4). Furthermore, the orthogonality of coordinates ξ and η in a quadrilateral element geometry allows for separation of variables and leads to efficiently implemented tensor products (see Appendix B1). Elemental integrals over (s,z) may now be mapped into (ξ,η) and discretized as

$$\int_{\Omega_e} u(s,z,t)\, s\, ds\, dz = \int_{-1}^{1}\int_{-1}^{1} u(s(\xi,\eta),z(\xi,\eta),t)s(\xi,\eta)\mathcal{J}(\xi,\eta)\, d\xi\, d\eta \approx \sum_{p,q=0}^{N} \sigma_p^N \sigma_q^N s(\xi_p,\eta_q)\mathcal{J}(\xi_p,\eta_q)u(\xi_p,\eta_q,t), \tag{11}$$

where $\sigma_{p,q} = \int_{-1}^{1} l_{p,q}^N(\xi)\, d\xi$ are the integration weights for non-axial elements. Time-dependent field variables such as the displacement are approximated as

$$u_\alpha(\xi,\eta,t) \approx \sum_{i,j=0}^{N} u_\alpha^{ij}(t) l_i^N(\xi) l_j^N(\eta), \tag{12}$$

where u_α stands for any of the components u_s, u_z, u_ϕ, or $u_\pm$. The coefficients $u_\alpha^{ij}(t)$ carry the actual function values at the nodes (ξ_i, η_j). Similarly, we define test functions w_β as

$$w_\beta(\xi,\eta) \approx \sum_{I,J=0}^{N} w_\beta^{IJ} l_I^N(\xi) l_J^N(\eta), \tag{13}$$

where β is the analogue of α for test functions. We set the coefficients w_β^{IJ} in the discretized version of eqs (5)–(7) equal to zero for all points except (ξ_I, η_J), effectively cancelling the summation and replacing elemental integrations with quantities defined at each point (I, J). For the remainder of the paper, we will adhere to the index convention (I, J, β) for test functions, (i, j, α) for displacements, and (p, q) arising from the quadrature. Using eqs (9) and (10), derivatives are expanded, for example, as

$$\partial_s u(s(\xi,\eta),z(\xi,\eta)) \approx \left[\partial_\eta z(\xi,\eta)\sum_{i,j=0}^{N}\partial_\xi l_i^N(\xi) l_j^N(\eta) u^{ij} - \partial_\xi z(\xi,\eta)\sum_{i,j=0}^{N} l_i^N(\xi)\partial_\eta l_j^N(\eta) u^{ij}\right]\mathcal{J}^{-1}(\xi,\eta). \tag{14}$$

In what follows, we will drop dependencies on t, (s,z), (ξ,η), and N for conciseness unless indispensable. We will also adopt the abbreviations $l_i'(\xi) = \partial_\xi l_i(\xi)$, $l_j'(\eta) = \partial_\eta l_j(\eta)$, and, for example, $s_\xi^{ij} = \partial_\xi s(\xi_i,\eta_j)$. Summation over I, J, i, j, and p, q always goes from 0 to N, unless otherwise noted. Each elemental integral term is computed by discretizing u_α and w_β, evaluating the integral with GLL quadrature, and recasting the system such that we obtain expressions over I, J as the free indices (see Section 4). For example, a typical term within the elemental monopole stiffness integral may be discretized as

$$\int_{\Omega_e} \lambda\, \partial_z w_z s^{-1} u_s s\, ds\, dz \approx \sum_{IJ} w_z^{IJ}\left[\sum_i -\lambda^{iJ}\sigma_i\sigma_J s_\eta^{iJ} l_I'(\xi_i) u_s^{iJ} + \sum_j \lambda^{Ij}\sigma_I\sigma_j s_\xi^{Ij} l_j'(\eta_j) u_s^{Ij}\right]. \tag{15}$$

We will elaborate upon the whole system in Section 4.4 and Appendix B.

3.3 Gauss–Lobatto–Jacobi (0,1) quadrature in axial elements

Particular attention must be focused on the elements adjacent to the axis for which the case $s = 0$ needs to be addressed. A convenient remedy is to introduce an additional factor in the quadrature formulae, and apply L'Hospital's rule if needed. Consequently, while retaining the GLL quadrature in the η direction, we resort to a Gauss-Lobatto–Jacobi (GLJ) (0,1) quadrature rule in the ξ direction and introduce Lagrange interpolating functions $\bar{l}_i(\bar{\xi}_p)$ over the set of associated quadrature nodes $\bar{\xi}_p,\ 0 \le p \le N$ (e.g. Fournier *et al.* 2005; Bernardi *et al.* 1999, see Fig. 2 for the relative distribution of GLJ versus GLL points, and Appendix A3 for definitions). Elemental integrals within axial elements are then expressed as

$$\int_{\bar{\Omega}_e} u\,(s,z)\, s\, ds\, dz \approx \sum_{pq} \bar{\sigma}_p (1+\bar{\xi}_p)^{-1}\sigma_q s(\bar{\xi}_p,\eta_q)\mathcal{J}(\bar{\xi}_p,\eta_q)u(\bar{\xi}_p,\eta_q). \tag{16}$$

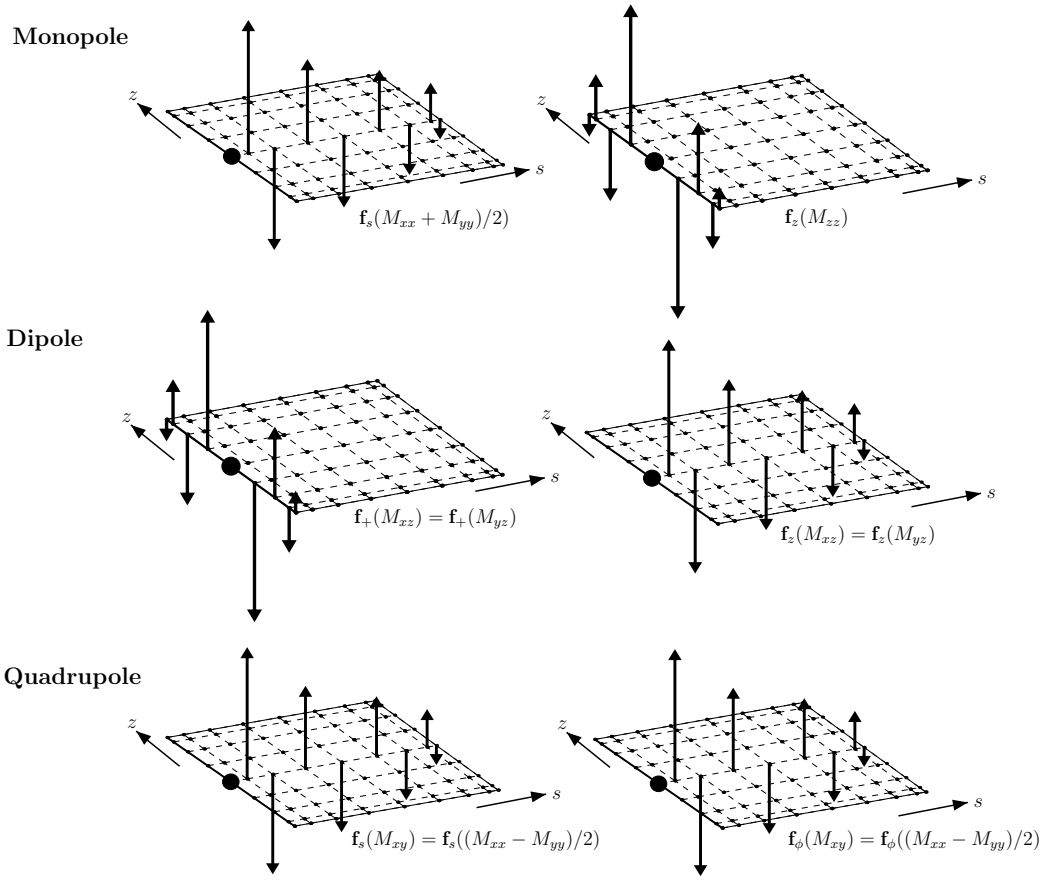

Figure 2. Moment-tensor source gallery. Due to the polynomial representation of functions in the spectral-element method, a point-like moment-tensor source, containing $\boldsymbol{\nabla}\mathbf{w}$, spreads out over the bearing element in its discretized form. The figure shows all non-zero source vector components $\mathbf{f}_\beta$ as defined in eqs (24)–(30) for the element containing the source at polynomial order $N = 8$. Arrow lengths represent the relative values of the magnitude of $\mathbf{f}_\beta$. The physical source location on the axis $s = 0$ is denoted by a large black dot. Neighbouring elements (not shown) share the same values as the edge of the shown element, thus a maximum of four elements may have non-zero source terms. Note that the location and relative spacing of grid points within the element is different for directions parallel and perpendicular to the axis, reflecting the axial discretization in terms of GLJ points for the ξ (and s) directions, and GLL points for the η (and z) directions (see Sections 3.2, 3.3 and Appendices A2, A3).

This definition introduces the singular term $(1+\bar{\xi}_p)^{-1}$ on the axis $\bar{\xi}_0 = -1$, which can be removed by applying L'Hospital's rule $s(\bar{\xi}_0, \eta_j)(1+\bar{\xi}_0)^{-1} = s_\xi^{0j}$. When evaluating stiffness integral expressions, we also make use of the axial identities $\bar{l}_i(\bar{\xi}_0)(1+\bar{\xi}_0)^{-1} = \partial_{\bar{\xi}}\bar{l}_i(\bar{\xi}_0)$, $z_\eta|_{s=0} = (\mathcal{J}s_\xi^{-1})|_{s=0}$ and $\partial_s u|_{s=0} = s^{-1}\,u|_{s=0}$ if $u|_{s=0} = 0$. For each integrand in eqs (5)–(7), we need to honour the two cases $p > 0$ and $p = 0$. For the latter location on the axis, L'Hospital's rule is invoked to evaluate terms involving s^{-1}. Similarly to the non-axial case, we obtain for example

$$\int_{\bar{\Omega}_e} \lambda\,\partial_z w_z s^{-1} u_s s\,ds\,dz \approx \sum_{IJ} w_z^{IJ}\Bigg[\sum_i -\lambda^{iJ}\bar{\sigma}_i\sigma_J(1+\bar{\xi}_i)^{-1}s_\eta^{iJ}\bar{l}_I'(\bar{\xi}_i)u_s^{iJ} + \sum_j \lambda^{Ij}\bar{\sigma}_I\sigma_j(1+\bar{\xi}_I)^{-1}s_\xi^{Ij}l_J'(\eta_j)u_s^{Ij}$$
$$+\sum_j \bar{\sigma}_0\sigma_j\lambda^{0j}s_\xi^{0j}\bar{l}_I'(\bar{\xi}_0)l_J'(\eta_j)u_s^{0j}\Bigg] + \sum_J w_z^{0J}\Bigg[\bar{\sigma}_0\sigma_J\lambda^{0J}s_\xi^{0J}\sum_i \bar{l}_i'(\bar{\xi}_0)\sum_j l_J'(\eta_j)u_s^{ij}\Bigg]. \tag{17}$$

The two terms in the second row appear due to the singularity removal via L'Hospital's rule; the first depends upon the displacement along the axis and contributes to the whole element w^{IJ}, whereas the second depends on the displacement in the whole element and appears only on the axis w^{0J}. Depending on the essential boundary condition, maximally one of these two terms is non-zero since in all cases either $w^{0J} = 0$ or $u^{0j} = 0$ for this type of integral. Section 4.4 contains details on the different terms and the full stiffness system is derived in Appendix B.

4 DISCRETIZED EQUATIONS OF MOTION

In this section, we will present the equations of motion for the multipole source system in discretized form, elaborate the scheme for time marching, and present the expanded expressions for all terms involved. Upon inserting eqs (12) and (13) into the equations of motion (5)–(7), we obtain a system of ordinary differential equations in time for each element

$$\sum_{IJ}\sum_\beta w_\beta^{IJ}\Bigg[\sum_{ij}\sum_\alpha M_{\beta\alpha}^{IJij}\ddot{u}_\alpha^{ij}(t) + \sum_{ij}\sum_\alpha K_{\beta\alpha}^{IJij}u_\alpha^{ij}(t)\Bigg] = \sum_{IJ}\sum_\beta w_\beta^{IJ} f_\beta^{IJ}(t), \tag{18}$$

where a double dot denotes the second partial derivative with respect to time, f_β^{IJ} are the expansion coefficients of the source term, and we abbreviated the elemental mass matrix by $M_{\beta\alpha}^{IJij}$ and the elemental stiffness matrix by $K_{\beta\alpha}^{IJij}$. In matrix notation, let $\mathbf{K}_e$ now be such a stiffness matrix of element e. We may then merge these elemental (local) contributions to a block-diagonal matrix $\mathbf{K}_\mathrm{L}$ (unassembled, global stiffness matrix) defined by

$$\mathbf{K}_\mathrm{L} = \begin{pmatrix} \mathbf{K}_1 & & & & & \\ & \ddots & & & & \\ & & \mathbf{K}_n & & & \\ & & & \bar{\mathbf{\Gamma}}\bar{\mathbf{K}}_1\bar{\mathbf{\Gamma}} & & \\ & & & & \ddots & \\ & & & & & \bar{\mathbf{\Gamma}}\bar{\mathbf{K}}_{\bar{n}}\bar{\mathbf{\Gamma}} \end{pmatrix}, \tag{19}$$

where $\bar{\mathbf{\Gamma}}$ is the diagonal matrix that acts as a 'mask' to set all components to zero which vanish on the axis in accordance with the essential axial boundary conditions eq. (4) (Nissen-Meyer *et al.* 2007; Fournier *et al.* 2004; Bernardi *et al.* 1999). We associate with each distinct node (i.e. counting nodes at $\xi, \eta = -1, 1$ only once) in Ω a unique global number (Deville *et al.* 2002) upon which we define the global displacement $\mathbf{u}$. We shall always use sans serif font to refer to global matrices of this assembled form. A Boolean connectivity matrix $\mathbf{Q}$ mapping $\mathbf{u}$ to $\mathbf{u}_\mathrm{L}$, i.e. $\mathbf{u}_\mathrm{L}$=$\mathbf{Q}\mathbf{u}$, copies values from the global vector into the collection of local vectors ('scatter'). The transpose operation $\mathbf{Q}^\mathrm{T}$ ('gather') sums up element edge/corner contributions. The joint application of $\mathbf{Q}\ \mathbf{Q}^\mathrm{T}$ is called the direct stiffness summation and constitutes the stiffness assembly stage; we denote the global, assembled stiffness matrix as $\mathbf{K} = \mathbf{Q}^\mathrm{T}\mathbf{K}_\mathrm{L}\mathbf{Q}$. Summing over all elemental stiffness terms $w_\beta^{ij} K_{\beta\alpha}^{IJij} u_\alpha^{ij}$ as in eq. (18), we write

$$\sum_{e=1}^{n+\bar{n}} \mathbf{w}_e^\mathrm{T}\mathbf{K}_e\mathbf{u}_e = \mathbf{w}_\mathrm{L}^\mathrm{T}\mathbf{K}_\mathrm{L}\mathbf{u}_\mathrm{L} = \mathbf{w}^\mathrm{T}\mathbf{Q}^\mathrm{T}\mathbf{K}_\mathrm{L}\mathbf{Q}\mathbf{u} = \mathbf{w}^\mathrm{T}\mathbf{K}\mathbf{u}. \tag{20}$$

The same concept applies to the mass and source terms $\mathbf{M}_\mathrm{L}$ and $\mathbf{f}_\mathrm{L}$. Construction of a global coordinate mesh and its relation to elemental nodes are based upon a global numbering technique (Deville *et al.* 2002). To obtain the semi-discretized version of eqs (5)–(7), we span the discrete space of test functions by setting each $\mathbf{w}$ to 1 at a specific grid point, and zero everywhere else. We can then drop summations over (I, J) and β to form an assembled, linear algebraic system of ordinary differential equations in time

$$\mathbf{M}\ddot{\mathbf{u}}(t) + \mathbf{K}\mathbf{u}(t) = \mathbf{f}(t). \tag{21}$$

4.1 Time marching

We solve the global system eq. (21) by an explicit acceleration-driven Newmark scheme of second-order accuracy (Chaljub & Valette 2004). If Δt denotes the time-step size, then the displacement, acceleration and velocity fields at time $t + \Delta t$ can successively be calculated from their values at time t as

$$\begin{aligned} &\text{Step 1: } \mathbf{u}(t+\Delta t) = \mathbf{u}(t) + \Delta t\dot{\mathbf{u}}(t) + \tfrac{1}{2}\Delta t^2\ddot{\mathbf{u}}(t),\\ &\text{Step 2: } \ddot{\mathbf{u}}(t+\Delta t) = \mathbf{M}^{-1}\left[\mathbf{f}(t+\Delta t) - \mathbf{K}\mathbf{u}(t+\Delta t)\right],\\ &\text{Step 3: } \dot{\mathbf{u}}(t+\Delta t) = \dot{\mathbf{u}}(t) + \tfrac{1}{2}\Delta t\left[\ddot{\mathbf{u}}(t) + \ddot{\mathbf{u}}(t+\Delta t)\right], \end{aligned} \tag{22}$$

with initial conditions $\mathbf{u}(0) = \mathbf{0}$, $\dot{\mathbf{u}}(0) = \mathbf{0}$, and $\ddot{\mathbf{u}}(0) = \mathbf{0}$. This scheme is conditionally stable, subject to the stability criterion ('Courant-Friedrichs-Levy Condition')

$$\Delta t < \mathcal{C} \min_\Omega \left(\frac{h}{v_\mathrm{p}}\right), \tag{23}$$

where h is the distance between neighbouring nodes, v_p the P wave velocity, and $\mathcal{C}$ the Courant number, which depends upon the dimensionality, order of the scheme and mesh geometry, and is empirically chosen to be between 0.3–0.6 (e.g. Komatitsch & Tromp 2002a). The scheme eq. (22) will prove useful when including fluid regions since it is fully explicit, avoiding iterations over boundary integrals (compare Komatitsch & Tromp 2002a, Section 3.7). The stiffness matrix is never computed itself, but rather only its action on the displacement $\mathbf{K}\mathbf{u}$. Note that, in the context of computing sensitivity kernels, the velocity $\dot{\mathbf{u}}$ is an intrinsic field variable and the strain tensor $\frac{1}{2}(\boldsymbol{\nabla}\mathbf{u} + (\boldsymbol{\nabla}\mathbf{u})^\mathrm{T})$ comes at a minimal cost to compute from the stiffness terms. The bulk computational effort is concentrated in step 2, specifically the stiffness term. We will now successively describe the different unassembled terms $\mathbf{f}$, $\mathbf{M}_\mathrm{L}\ddot{\mathbf{u}}_\mathrm{L}$, and $\mathbf{K}_\mathrm{L}\mathbf{u}_\mathrm{L}$ involved in step 2 at the elemental level.

4.2 Source terms

Due to the inherent cylindrical symmetry, point sources are always located on the axis such that $\mathbf{r}_\mathrm{s} = r_\mathrm{s}\hat{\mathbf{z}}$ for moment tensors and $\mathbf{r}_\mathrm{r} = r_\mathrm{r}\hat{\mathbf{z}}$ for point forces. We additionally assume here that sources coincide with mesh nodes which is not a compulsory limitation of the method, but will suffice for immediate purposes. Discretized moment-tensor source terms effectively get 'spread out' over the bearing element due to

the polynomial representation of the $\boldsymbol{\nabla}\mathbf{w}$ operation, as can be verified from the sum appearing in terms such as eq. (14). Point forces $p_{x,y,z}$ on the other hand remain non-zero only at $\mathbf{r}_\mathrm{r} = (0, r_\mathrm{r})$. We compute the non-zero components f_β of the respective source types appearing in eqs (5)–(7) for the monopole as

$$f_z^{IJ}(p_z, t) = (2\pi)^{-1}\delta_{I0}\delta_{JJ_\mathrm{r}}\delta(t), \tag{24}$$

$$f_z^{IJ}(M_{zz}, t) = (2\pi)^{-1}M_0\delta_{I0}l'_J(\eta_\mathrm{s})z_\eta^{0J_\mathrm{s}}H(t), \tag{25}$$

$$f_s^{IJ}((M_{xx} + M_{yy})/2, t) = (2\pi)^{-1}M_0\delta_{JJ_\mathrm{s}}(1-\delta_{I0})\bar{l}'_I(\bar{\xi}_0)s_\xi^{0J_\mathrm{s}}H(t), \tag{26}$$

for the dipole as

$$f_+^{IJ}(p_x, t) = f_+^{IJ}(p_y, t) = \pi^{-1}\delta_{I0}\delta_{JJ_\mathrm{r}}\delta(t), \tag{27}$$

$$f_+^{IJ}(M_{xz}, t) = f_+^{IJ}(M_{yz}, t) = \pi^{-1}\delta_{I0}l'_J(\eta_\mathrm{s})z_\eta^{0J_\mathrm{s}}H(t), \tag{28}$$

$$f_z^{IJ}(M_{xz}, t) = f_z^{IJ}(M_{yz}, t) = \pi^{-1}M_0\delta_{JJ_\mathrm{s}}(1-\delta_{I0})\bar{l}'_I(\bar{\xi}_0)s_\xi^{0J_\mathrm{s}}H(t), \tag{29}$$

and for the quadrupole as

$$f_{s,\phi}^{IJ}(M_{xy}, t) = f_{s,\phi}^{IJ}((M_{xx} - M_{yy})/2, t) = \pi^{-1}M_0\delta_{JJ_\mathrm{s}}(1-\delta_{I0})\bar{l}'_I(\bar{\xi}_0)s_\xi^{0J_\mathrm{s}}H(t), \tag{30}$$

where M_0 is the scalar moment. Fig. 2 illustrates the spatial distribution of functions f_β^{IJ} for the moment-tensor sources to emphasize the spreading of the source representation across the whole element. The actual physical source location (large black dot) has zero source-vector amplitude. Note also that up to three elements neighbouring the source element carry non-zero values as assembled from the element edges shared with the source-bearing element.

4.3 Mass terms

The mass matrix is diagonal by construction and, therefore, readily invertible. One can deduce from eq. (11) that the mass terms of non-axial elements (as in eq. 18) take the form for monopole sources,

$$\sum_{ij}\sum_{\alpha}\left(M_{s\alpha}^{IJij} + M_{z\alpha}^{IJij}\right)\ddot{u}_\alpha^{ij} = \rho^{IJ}\sigma_I\sigma_J s^{IJ}\mathcal{J}^{IJ}\left(\ddot{u}_s^{IJ} + \ddot{u}_z^{IJ}\right), \tag{31}$$

for dipole sources,

$$\sum_{ij}\sum_{\alpha}\left(M_{+\alpha}^{IJij} + M_{-\alpha}^{IJij} + M_{z\alpha}^{IJij}\right)\ddot{u}_\alpha^{ij} = \rho^{IJ}\sigma_I\sigma_J s^{IJ}\mathcal{J}^{IJ}\left(2\ddot{u}_+^{IJ} + 2\ddot{u}_-^{IJ} + \ddot{u}_z^{IJ}\right), \tag{32}$$

and for quadrupole sources,

$$\sum_{ij}\sum_{\alpha}\left(M_{s\alpha}^{IJij} + M_{\phi\alpha}^{IJij} + M_{z\alpha}^{IJij}\right)\ddot{u}_\alpha^{ij} = \rho^{IJ}\sigma_I\sigma_J s^{IJ}\mathcal{J}^{IJ}\left(\ddot{u}_s^{IJ} + \ddot{u}_\phi^{IJ} + \ddot{u}_z^{IJ}\right). \tag{33}$$

The factors preceding the acceleration components are statically pre-computed and inverted, hence the operation $\mathbf{M}^{-1}$ in step 2 of eq. (22) is merely a point-by-point multiplication. The axial case is equivalent after the substitution $\sigma_I \to \bar{\sigma}_I(1+\bar{\xi}_I)^{-1}$ and application of L'Hospital's rule on the axis: $s^{0J}(1+\bar{\xi}_0)^{-1} = (\partial_\xi s)^{0J}$.

4.4 Stiffness terms

We relegate the description of the composite stiffness term to Appendix B and only sketch the solution to the different types of integrals here. Discretization yields a number of pre-computable quantities A, B, C, D, and G which are collectively defined in Table 1 for axial and non-axial elements using the definitions in Section 3.2 and the axial expressions from Section 3.3. The terms involved in the stiffness matrix are computationally most demanding and need to be optimized. The two contributing factors of (i) recasting terms to avoid repeated operations and (ii) usage of cache-access optimized tensor products are explained in Appendix B. Here, we simply depict the different types of integrals, for example, for non-axial elements

$$\int_{\Omega_e}\epsilon\frac{w_\beta}{s}\frac{u_\alpha}{s}s\,ds\,dz \approx \sum_{IJ}w_\beta^{IJ}\left({}_\epsilon A^{IJ}u_\alpha^{IJ}\right) = \sum_{IJ}w_\beta^{IJ}\left(R_1^\alpha\right)^{IJ}, \tag{34}$$

$$\int_{\Omega_e}\epsilon\frac{w_\beta}{s}\partial_x u_\alpha s\,ds\,dz \approx \sum_{IJ}w_\beta^{IJ}\left({}_\epsilon B_{\chi_\eta}^{IJ}\sum_i D_\xi^{iI}u_\alpha^{iJ} + {}_\epsilon B_{\chi_\xi}^{IJ}\sum_j D_\eta^{jJ}u_\alpha^{Ij}\right) = \sum_{IJ}w_\beta^{IJ}\left(R_2^\alpha\right)^{IJ}, \tag{35}$$

$$\int_{\Omega_e}\epsilon\partial_x w_\beta\frac{u_\alpha}{s}s\,ds\,dz \approx \sum_{IJ}w_\beta^{IJ}\left(\sum_i {}_\epsilon B_{\chi_\eta}^{iJ}D_\xi^{Ii}u_\alpha^{iJ} + \sum_j {}_\epsilon B_{\chi_\xi}^{Ij}D_\eta^{Jj}u_\alpha^{Ij}\right) = \sum_{IJ}w_\beta^{IJ}\left(R_3^\alpha\right)^{IJ}, \tag{36}$$

Table 1. Definitions for pre-computable matrices of the stiffness term ($\epsilon = \lambda$, μ or any combination thereof).

Matrix	Non-axial elements	Axial elements ($i > 0$)	Axial elements ($i = 0$)	
${}_\epsilon A^{ij}$	$\epsilon^{ij}\sigma_i\sigma_j(s^{ij})^{-1}\mathcal{J}^{ij}$	$\epsilon^{ij}\bar{\sigma}_i(1+\bar{\xi}_i)^{-1}\sigma_j(s^{ij})^{-1}\mathcal{J}^{ij}$	${}_\epsilon A^{0j} = \epsilon^{0j}\bar{\sigma}_0\sigma_j\mathcal{J}^{0j}(s_\xi^{0j})^{-1}$	
${}_\epsilon B_{z_\eta}^{ij}$	$\epsilon^{ij}\ \sigma_i\sigma_j\ z_\eta^{ij}$	$\epsilon^{ij}\bar{\sigma}_i(1+\bar{\xi}_i)^{-1}\sigma_j z_\eta^{ij}$	${}_\epsilon B_{z_\eta}^{0j} = \epsilon^{0j}\bar{\sigma}_0\sigma_j z_\eta^{0j} = {}_\epsilon A^{0j}$	
C^{ij}	$\sigma_i\sigma_j s^{ij}(\mathcal{J}^{ij})^{-1}$	$\bar{\sigma}_i\sigma_j s^{ij}(1+\bar{\xi}_i)^{-1}(\mathcal{J}^{ij})^{-1}$	$C^{0j} = \bar{\sigma}_0\sigma_j s_\xi^{0j}(\mathcal{J}^{0j})^{-1}$	
D_ξ^{Ii}	$\partial_\xi l_I(\xi_i)$	$\partial_\xi \bar{l}_I(\bar{\xi}_i)$	$\partial_\xi \bar{l}_I(\bar{\xi}_0)$	
D_η^{Jj}	$\partial_\eta l_J(\eta_j) = \partial_\xi l_J(\xi_j)$	$\partial_\eta l_J(\eta_j)$		
$(G_k^{xy})^{ij}$	$k=1$	$k=2$	$k=3$	$k=4$
$x=s, y=s$	$z_\xi^{ij}\ z_\eta^{ij}$	$z_\eta^{ij}\ z_\eta^{ij}$	$z_\xi^{ij}\ z_\eta^{ij}$	$z_\xi^{ij}\ z_\xi^{ij}$
$x=s, y=z$	$z_\xi^{ij}\ s_\xi^{ij}$	$z_\eta^{ij}\ s_\eta^{ij}$	$z_\xi^{ij}\ s_\eta^{ij}$	$z_\xi^{ij}\ s_\xi^{ij}$
$x=z, y=s$	$s_\eta^{ij}\ z_\xi^{ij}$	$s_\eta^{ij}\ z_\eta^{ij}$	$s_\xi^{ij}\ z_\eta^{ij}$	$s_\xi^{ij}\ z_\xi^{ij}$
$x=z, y=z$	$s_\xi^{ij}\ s_\eta^{ij}$	$s_\eta^{ij}\ s_\eta^{ij}$	$s_\xi^{ij}\ s_\eta^{ij}$	$s_\xi^{ij}\ s_\xi^{ij}$

$$\int_{\Omega_e} \epsilon\partial_x w_\beta \partial_y u_\alpha s\,ds\,dz \approx \sum_{IJ} w_\beta^{IJ}\Bigg[\sum_i D_\xi^{Ii}C^{iJ}\big(G_1^{xy}\big)^{iJ}\sum_j D_\eta^{jJ}u_\alpha^{ij} + \sum_p D_\xi^{Ip}C^{pJ}\big(G_2^{xy}\big)^{pJ}\sum_i D_\xi^{ip}u_\alpha^{iJ} + \sum_j D_\eta^{Jj}C^{Ij}(G_3^{xy})^{Ij}\sum_i D_\xi^{iI}u_\alpha^{ij} + \sum_q D_\eta^{Jq}C^{Iq}\big(G_4^{xy}\big)^{Iq}\sum_j D_\eta^{jq}u_\alpha^{Ij}\Bigg] = \sum_{IJ} w_\beta^{IJ}\big(R_4^\alpha\big)^{IJ}, \tag{37}$$

where the pre-computed matrices A^{ij}, $B_{\chi_\xi}^{ij}$, C^{ij} as given in Table 1 may generally contain integration weights, the Jacobian, mapping derivatives, the coordinate s, and elastic parameters. If $\partial_x = \partial_s$ then $\chi = z$, and if $\partial_x = \partial_z$ then $\chi = s$. We abbreviated the quantities in brackets as $(R_k^\alpha)^{IJ}$, which contain the actual operations to be carried out to obtain **Ku**, the stiffness matrix acting on the displacement. In addition, we collected twice-appearing mapping derivatives into $(G_k^{xy})^{ij}$, defined in Table 1. Inspecting the equations of motion (5)–(7), we note that whenever factors $s^{-1}\ w_\beta$ appear, w_β vanishes at the axis; and equivalently for u_α. Thus, a number of sums are developed for the two cases $I > 0$ and $I = 0$, resulting in summation for $I > 0$ and additional terms for $I = 0$. An equivalent scenario prevails for u_α and the corresponding summation over i. The respective integrals for axial elements are then approximated as

$$\int_{\bar{\Omega}^e} \epsilon\frac{w_\beta}{s}\frac{u_\alpha}{s}s\,ds\,dz \approx \sum_{I>0\,J} w_\beta^{IJ}\left({}_\epsilon A^{IJ}u_\beta^{IJ} + D_\xi^{I0}A^{0J}\sum_{i>0} D_\xi^{i0}u_\beta^{iJ}\right) = \sum_{I>0\,J} w_\beta^{IJ}\big(\bar{R}_1^\alpha\big)^{IJ}, \tag{38}$$

$$\int_{\bar{\Omega}^e} \epsilon\frac{w_\beta}{s}\partial_x u_\alpha s\,ds\,dz \approx \sum_{I>0\,J} w_\beta^{IJ}\left[{}_\epsilon B_{\chi_\eta}^{IJ}\sum_i D_\xi^{iI}u_\alpha^{iJ} + {}_\epsilon B_{\chi_\xi}^{IJ}\sum_j D_\eta^{jJ}u_\alpha^{Ij} + \bar{L}_1(u_\alpha)^{IJ}\right] = \sum_{I>0\,J} w_\beta^{IJ}\big(\bar{R}_2^\alpha\big)^{IJ}, \tag{39}$$

$$\int_{\bar{\Omega}^e} \epsilon\partial_x w_\beta\frac{u_\alpha}{s}s\,ds\,dz \approx \sum_{IJ} w_\beta^{IJ}\left[\sum_{i>0}{}_\epsilon B_{\chi_\eta}^{iJ}D_\xi^{Ii}u_\alpha^{iJ} + \sum_j{}_\epsilon B_{\chi_\xi}^{Ij}D_\eta^{Jj}u_\alpha^{Ij} + \bar{L}_2(u_\alpha)^{IJ}\right] = \sum_{IJ} w_\beta^{IJ}\big(\bar{R}_3^\alpha\big)^{IJ}, \tag{40}$$

$$\int_{\bar{\Omega}^e} \epsilon\partial_x w_\beta \partial_y u_\alpha s\,ds\,dz \approx \sum_{IJ} w_\beta^{IJ}\Bigg[\sum_i D_\xi^{Ii}C^{iJ}\big(G_1^{xy}\big)^{iJ}\sum_j D_\eta^{jJ}u_\alpha^{ij} + \sum_p D_\xi^{Ip}C^{pJ}(G_2^{xy})^{pJ}\sum_i D_\xi^{ip}u_\alpha^{iJ} + \sum_j D_\eta^{Jj}C^{Ij}\big(G_3^{xy}\big)^{Ij}\sum_i D_\xi^{iI}u_\alpha^{ij} + \sum_q D_\eta^{Jq}C^{Iq}\big(G_4^{xy}\big)^{Iq}\sum_j D_\eta^{jq}u_\alpha^{Ij}\Bigg] = \sum_{IJ} w_\beta^{IJ}\big(\bar{R}_4^\alpha\big)^{IJ}. \tag{41}$$

We do not explicitly differentiate between axial and non-axial pre-computed matrices of Table 1 but rather acknowledge that the usage automatically conforms with the respective definitions. The additional terms $\bar{L}_{1,2}^{IJ}$ depend on the direction of the derivative:

$$\text{Case } \partial_x = \partial_s: \quad \bar{L}_1(u_\alpha)^{IJ} = \bar{L}_2(u_\alpha)^{IJ} = D_\xi^{I0}{}_\epsilon A^{0J}\sum_i D_\xi^{i0}u_\alpha^{iJ}, \tag{42}$$

$$\text{Case } \partial_x = \partial_z: \quad \bar{L}_1(u_\alpha)^{IJ} = D_\xi^{I0}{}_\epsilon B_{s_\xi}^{0J}\sum_j D_\eta^{jJ}u_\alpha^{0j} + {}_\epsilon B_{s_\xi}^{0J}\sum_j D_\eta^{jJ}\sum_i D_\xi^{i0}u_\alpha^{ij}, \tag{43}$$

$$\bar{L}_2(u_\alpha)^{IJ} = D_\xi^{I0}\sum_j D_\eta^{Jj}{}_\epsilon B_{s_\xi}^{0j}u_\alpha^{0j} + \sum_j D_\eta^{Jj}{}_\epsilon B_{s_\xi}^{0j}\sum_{i>0} D_\xi^{i0}u_\alpha^{ij}. \tag{44}$$

Since $z_\xi|_{s=0} = s_\eta|_{s=0} = 0$, there are no terms involving $B^{0j}_{z\xi}$ and $B^{0j}_{s\eta}$. Also note that in the case of ∂_z (eqs 43–44), the respective former term depends upon the displacement along the axis and contributes to the whole axial element in $(\bar{R}^\alpha_{(2,3)})^{IJ}$, whereas the latter term is synthesized from the displacement in the whole element and only inhabits the axis within $(\bar{R}^\alpha_{(2,3)})^{0J}$. Hence if, for example, $u_\alpha|_{s=0} = w_\beta|_{s=0} = 0$, then there is no additional axial term for $\partial_x = \partial_z$, i.e. $\bar{L}_1 = \bar{L}_2 = 0$. The expressions $(R^\alpha_k)^{IJ}$ and $(\bar{R}^\alpha_k)^{IJ}$ are the building blocks for the discretized stiffness term, subject to rearrangement and tensorization for optimization purposes. All details are discussed in Appendix B. In summary, the stiffness term is approximated as follows:

(i) Axial masking of displacement **u**,
(ii) Computation of elemental stiffness terms **Ku**,
(iii) Axial masking of **Ku**,
(iv) Assembly to obtain **Ku**.

5 NUMERICAL VALIDATION

In the remainder of the paper, we will examine a homogeneous sphere with $v_\mathrm{p} = 10\,\mathrm{km\,s^{-1}}$, $v_\mathrm{s} = 5.77\,\mathrm{km\,s^{-1}}$, and $\rho = 3000\,\mathrm{kg\,m^{-3}}$. For the purpose of a reliable validation of all relevant aspects of the method as discussed in Section 4, we separately address the stiffness and mass terms, the source terms and full-wave propagation. We will commence with an elastostatic comparison with the analytical toroidal eigenfunctions to constrain the accuracy of the dipole and quadrupole stiffness terms, followed by an explosion source simulation to examine the emanating wavefield in the source vicinity using an exact analytical solution and lastly, we show globally distributed seismograms along with solutions from normal-mode summation, and associated energy conservation of the scheme.

5.1 Spatial accuracy: toroidal eigenfunctions

The most complex and computationally intense part of the algorithm is the stiffness term, as detailed in Appendix B. In this section, we specifically validate its implementation by solving the source-free elastostatic wave equation. While the full-wave propagation problem is of a different nature and complication, we recall that our sought solution is the entire 2-D wavefield to be stored for the computation of sensitivity kernels, which motivates us to elaborate on the accuracy over the whole domain, rather than at selected stations at the surface. To this end, this test enables an easy computation of the residual misfit for the spatial discretization of the scheme at every grid point. The toroidal eigenfunctions (see Appendix C for a derivation and illustration) compose the displacement field **u** as a solution to the elastostatic problem, allowing for variable resolution by changing the degree l and overtone n. In the interest of simplicity, we restrict ourselves to the toroidal type. The resulting omission of the monopole case poses no major limitation since the quadrupole stiffness term embraces the full non-axial monopole term (see Table A2 and a number of the additional axial terms in eqs (B18) and (B19) and eqs (B26)–(B28). The validation lies in using the eigenfunction **u** for a given eigenfrequency ${}_n\omega_l$ to compute the assembled term $\mathbf{M}^{-1}(\mathbf{Ku})$ using our SEM as described in Section 4 and compare it to the equivalent reference term ${}_n\omega_l{}^2\mathbf{u}$ (see Appendix C). Fig. 3 exemplifies this concept via 1-D profiles of both the reference (dots) and SEM-based terms (solid lines) for various l and n, along the axis $s = 0$ in (D1) and (D2), the equator $z = 0$ in (Q1) and (Q2), the surface $r = r_0$ in (D3), and at fixed radii $r_1 = 2701$ km and $r_2 = 2931$ km in (D4)–(D6), (Q3) and (Q4) which are just above and below the middle coarsening level in Fig. 1 (c). Dots denote the location of grid points for polynomial order $N = 5$ as used in these simulations and components are shown in the spherical system $(\hat{\mathbf{r}}, \hat{\boldsymbol{\theta}}, \hat{\boldsymbol{\phi}})$ such that $\hat{\mathbf{r}}\cdot\mathbf{u} = 0$ for the toroidal case. (D1) is a simple, low-resolution case validating the axial representation of functions with sensitivity throughout all depths, hence sampling all variants of the mesh geometry, especially the central region, which is largely ignored by higher-degree eigenfunctions. (D2) shows the axial profile of the ϕ component for $l = n = 71$ which corresponds to more than one eigenfunction lobe per element, indicating very sparse sampling. Consequently, the approximation is slightly ragged, as shown in the magnified window which illustrates that 5 grid points per lobe are still sufficient to yield correct values at the grid points. A critical location for accuracy studies is any coarsening level, inasmuch as it encompasses a doubling in grid spacing. (D4) is a constant-depth, global profile of the ϕ components just above the central coarsening level, yielding a smooth and accurate representation of eigenfunctions, whereas profile (D5), extracted from just below the coarsening and hence consisting of half the number of grid points, shows large errors at local maxima due to the poor grid point density at $l = n = 51$. Decreased resolution ($l = n = 36$) in (D6) again yields acceptable results for that coarsened level. The same situation is underscored in (Q3)–(Q4) for the quadrupole θ component. (D3) on the other hand depicts a free-surface profile for $l = n = 71$ without imprecisions, adhering to the particularly dense element population at the surface. (Q2) verifies that the radial component vanishes, here along the equator for $l = n = 71$, which indicates that there will be no spurious radial modes numerically excited, for example, for insufficient grid resolution. In summary, typical spatial wavelengths need to be sampled by about ten grid points to guarantee a smooth representation of the waveform everywhere in the domain, as may be seen in (D2), (D5) and (Q3). The coarsening levels are subject to significant elemental distortion and hence most prone to inaccuracies, whereas the remaining domain by and large may well allow for fewer spatial points per wavelength. One may resort to placing each of the coarsening layers deeper than shown here to reach smaller grid spacings and errors. To quantify the overall accuracy, we compute the $\mathbb{L}^2$ norm of spatial residuals,

$$\ell_\mathrm{space} = \left\{ \frac{\int_\Omega \left[\mathbf{M}^{-1}(\mathbf{Ku}) - {}_n\omega_l^2\mathbf{u}\right]^2 d\Omega}{\int_\Omega \left({}_n\omega_l^2\mathbf{u}\right)^2 d\Omega} \right\}^{1/2}, \tag{45}$$

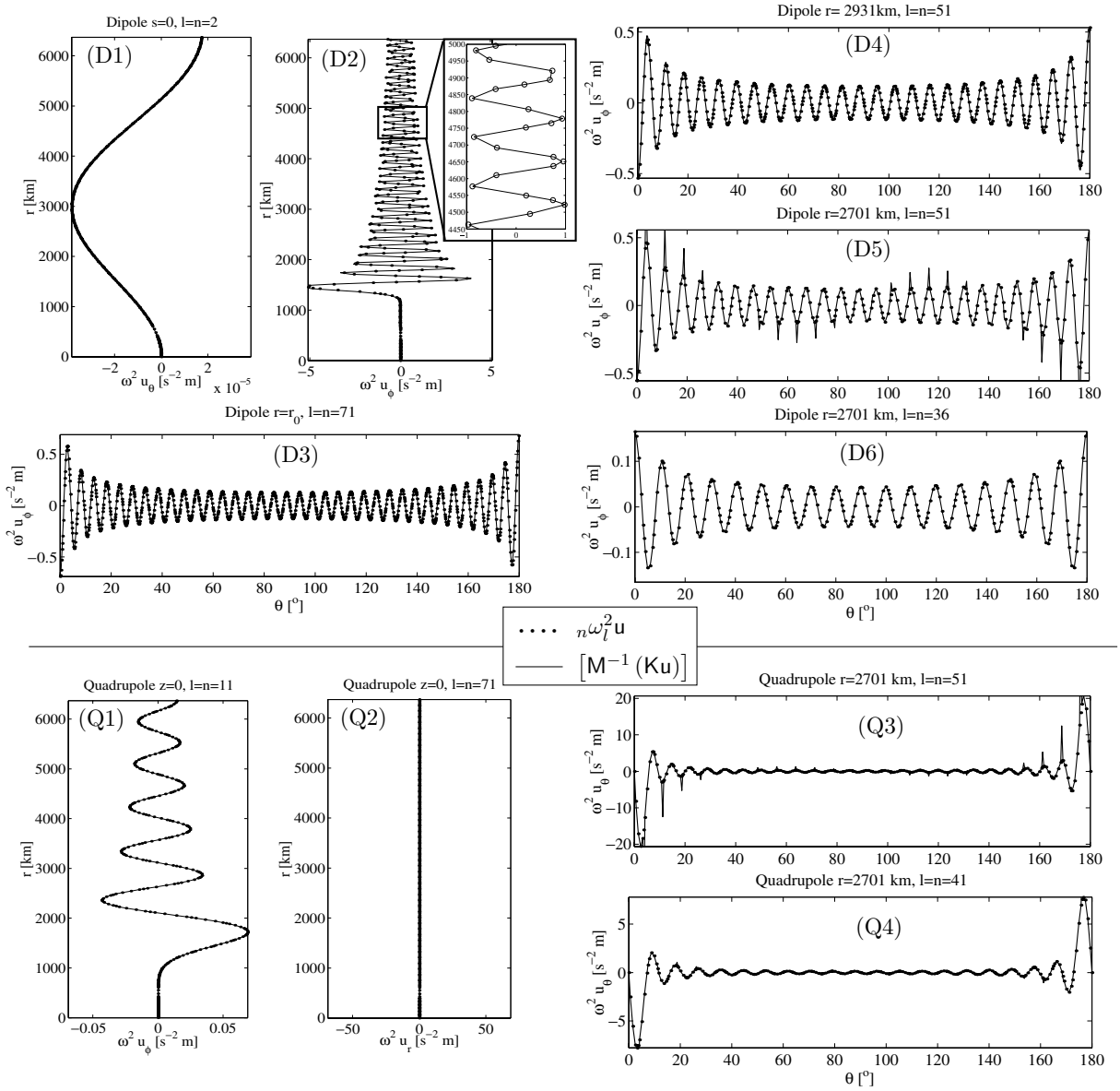

Figure 3. 1-D profiles of reference (dots) and SEM-based solutions (solid lines) to the elastostatic wave equation, based on toroidal eigenfunctions (Appendix C). The dots furthermore denote the location of grid points for polynomial order $N = 5$. The top panels (D1)–(D6) depict various cases for the dipole system, the bottom panels (Q1)–(Q4) depict the quadrupole. Choices of degree l and overtone n are given at the top of each panel, and the respective components are subscribed on axis labels. The profiles are along the axis $s = 0$ in (D1) and (D2), along the equator $z = 0$ in (Q1) and (Q2), along the free surface $r = r_0$ (D6), and at fixed radii $r_1 = 2701$ km and $r_2 = 2931$ km in (D3)–(D5) and (Q3)–(Q4). For (D2), we added a magnified window to illustrate the sparse grid point distribution. r_1 is the radius at which the grid spacing is (horizontally) maximal, that is, just beneath the middle grid coarsening in Fig. 1, and r_2 is just above that level.

as a function of polynomial order N, hence depicting the accuracy averaged across each grid point. This is shown in Fig. 4 for both the dipole (left) and quadrupole (right) excitation types. The function follows a quasi-linear trend indicative of spectral convergence, one of the merits of a spectral approach like the SEM. The accuracy varies by a few orders of magnitude depending on the choice of N or l, n. The graphs are cut off below 10^{-8} since spherical Bessel functions and eigenfrequencies (as needed for the eigenfunctions) are only computed to this precision. Since their stiffness systems differ significantly, it is noteworthy to recognize the striking similarity in accuracy for both dipole and quadrupole cases, suggesting a consistently accurate representation of all source types. To avoid inaccuracies such as in Fig. 3 (D5) and (Q3), we shall only accept values of $\ell_{\text{space}} < 10^{-3}$. Generally, it is expected that the overall error for seismic-wave propagation, i.e. including the temporal error stemming from the second-order time discretization to be addressed in Section 5.3, will exceed the spatial error computed here. Thus, rather than appointing a selective, even more stringent accuracy level, these spatial results mainly confirm the high convergence rate, correct implementation of all stiffness and mass terms, assembly and global numbering technique across each grid point of the mesh, including the free surface, coarsening levels and the axis $s = 0$. Furthermore, this validation technique may generally be useful for global solutions to

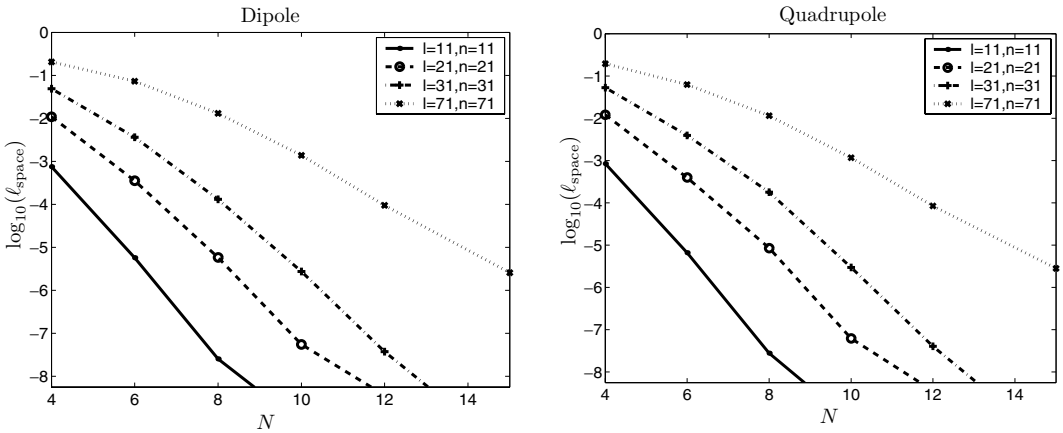

Figure 4. Global spatial convergence based upon toroidal eigenfunctions (see Appendix C). The $\mathbb{L}^2$ norm for the residual between reference and SEM solutions ℓ_{space} as defined in eq. (45), is shown as a function of the polynomial order N for four different choices of degree l and overtone n (left: dipole, right: quadrupole). The quasi-linearity on a semi-logarithmic plot is indicative of the expected spectral convergence. The reference solution depends upon spherical Bessel functions and the eigenfrequencies, which have been computed with an accuracy tolerance of about 10^{-8}. We only show errors above that margin. Note the striking similarity in accuracy for both dipole and quadrupole, given their differing stiffness terms.

the elastostatic variational problem, for example, as a thorough benchmark test for spatial accuracy, in that it is an easily implemented and computed test case to determine global accuracy and convergence properties.

5.2 The source vicinity: explosive radiation

Since one of the most significant aspects of our spectral-element method is the inclusion of a full 3-D moment tensor in a 2-D domain, we deem it important to zoom in to the source region. In this context, we conduct an accuracy study in the source vicinity, especially in light of computing kernels which depend upon the global and hence also near-source wavefield. The source element itself is expected to exhibit imprecise results due to the spatially spread-out moment-tensor representation (Section 4.2); for example, Faccioli *et al.* (1997) conclude that the wavefield resumes acceptable accuracy at least one wavelength away from the physical source location. Moreover, in 3-D SEM-based seismic-wave propagation, a spurious direct S wave from an explosion source has been observed and labelled as potentially resulting from the spread-out source representation (Schuberth 2003). We address all these issues by comparing with the exact analytical radiation for an explosion in a homogeneous medium, given by

$$u(r', t) = \frac{M_0}{4\pi\rho v_{\mathrm{p}}^2}\left[\frac{g\left(t-\frac{r'}{v_{\mathrm{p}}}\right)}{r'^2} + \frac{\dot{g}\left(t-\frac{r'}{v_{\mathrm{p}}}\right)}{r' v_{\mathrm{p}}}\right], \tag{46}$$

where $r' = |\mathbf{r} - \mathbf{r}_{\mathrm{s}}|$ is the distance from the source, $M_0 = 10^{20}$ Nm is the moment, and $g(t)$ is the source time function, here taken as a Gaussian $g(t) = \exp(-\gamma(t/T_0 - \tau)^2)$ with $\gamma = 12.25$, and $\tau = 1.5$ at a dominant period $T_0 = 70$ s. Note that eq. (46) is a purely radial displacement of a direct P wave. The explosion source $M_{xx} + M_{yy} + M_{zz}$ validates all variants of the moment tensor source types, inasmuch as it includes both generic derivatives $\partial_s w$ and $\partial_z w$ from eqs (5)–(7). Fig. 5 shows simulations of an explosion at $r_{\mathrm{s}} = 3835$ km using the mesh in Fig. 1 with polynomial order $N = 5$ and a time step $\Delta t = 0.25$ s, leading to a Courant number $\mathcal{C} = 0.37$. Snapshots in the source region at $t = 157.3$ s for the exact analytical (top left) and the SEM-based solutions (top centre) are indistinguishable for the propagating P wave but exhibit differences in the immediate source vicinity, as shown in two close-up plots of the elements around the source (black square). It is important to notice that not only the element containing the physical point source location bears a non-zero source vector field $\mathbf{f}$ (denoted by large black dots), but also some of the adjacent element edges, namely above, below and to the right for an explosion moment tensor. Labels 1–8 indicate the locations of the displacement time-series shown on the right along with their respective distances from the source in terms of dominant wavelengths of the P wave. All locations are well inside the near-field regime as can also be seen from the waveform shapes. The differences between the SEM and exact solutions gradually decrease from 1 to 4, yielding very good alignments at location 4, two elements away from the physical source location even if well less than one wavelength away. This means that we can obtain correct near-field representations, a potentially important feature for computing sensitivity kernels. This good agreement also validates the correct treatment of the axial boundary conditions and discretization, including the additional axial terms. As expected, waveforms 1–3, located between one and two elements away from the source, show more significant misfits, mainly in the amplitude. Time-series 5–8 show improved alignment at locations similar to 1–4 but away from the axis, especially at the second trace. This improvement may be caused by the asymmetric source term itself, with the physical location being closer to location 1 than 5. All these observations suggest that our source implementation is very well behaved when recording wavefields more than two elements away from the physical source location. In applications, the erroneous source elements may either be left out, or computed via analytical expressions such as eq. (46) for the explosion, assuming near-source constant material properties and no reflections. For any realistic earth-like parameter choice, the source elements will have a negligible influence on sensitivity kernels

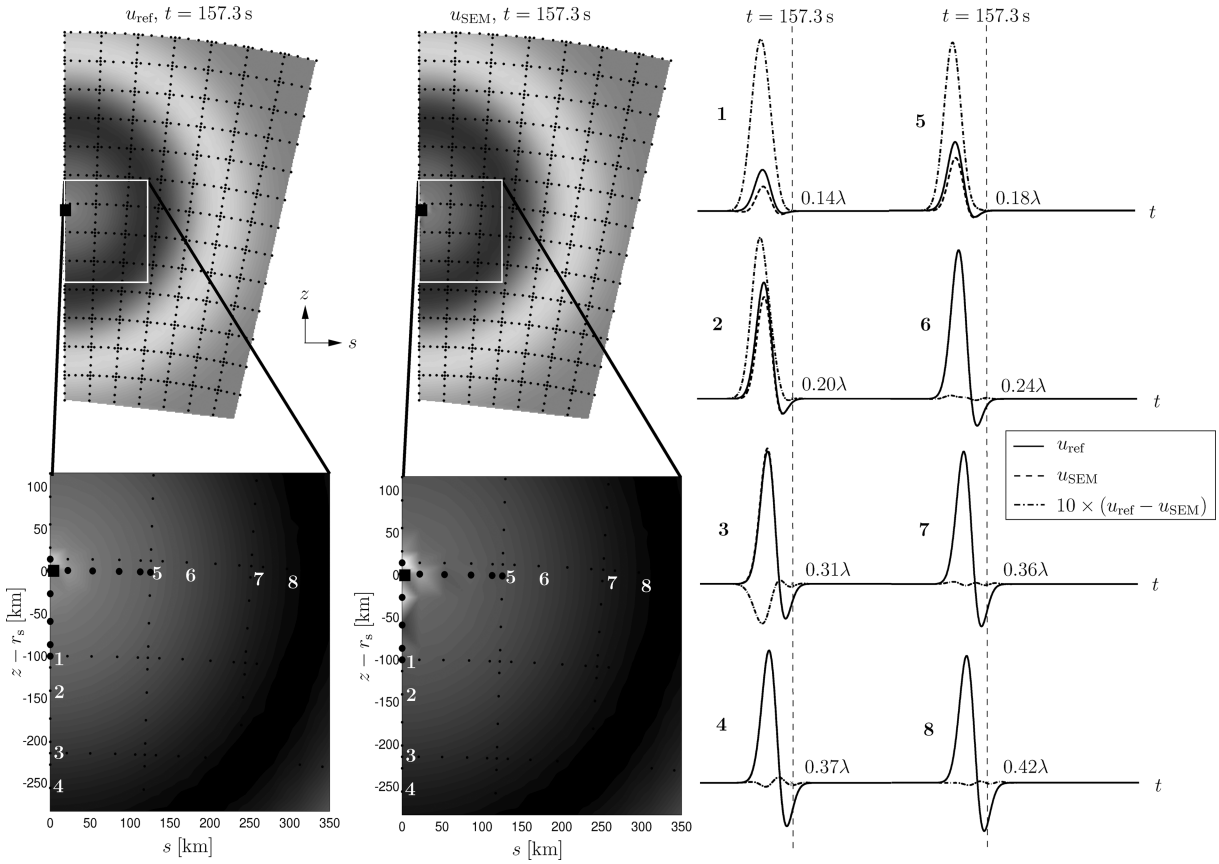

Figure 5. Explosion source radiation. Snapshots at $t = 157.3$ s are shown for both the reference (eq. 46, left) and the SEM-based solution (centre) for an explosion source at $r_s = 3835$ km with dominant period $T_0 = 70$ s. While the direct P wave away from the source is identical between both cases, one can observe differences in the immediate source vicinity. Seismograms labelled 1 to 4 represent locations downwards along the axis, and 5 to 8 are locations perpendicular from the axis as shown in the zoomed snapshots at the bottom left. The black square is the physical source location, large black dots are the non-zero source vector locations, small black circles denote (shared) element edges and corners. Analytical and SEM traces vastly differ within the source element, but are acceptably similar for trace 4. Fractions of λ depict respective distances in terms of dominant wavelengths, that is, all locations are still well inside the near-field regime. We conclude that the source-bearing elements are partly erroneous as expected, but one element away yields satisfactory results.

in a global sense, particularly when attention is focused on diffracted or triplicated phases. Furthermore, the spatial extent of these elements may well be within the source location uncertainty. Additionally, we do not observe any spurious shear motion trailing the compressional wave. Should any such phase exist, then it does not seem to directly originate in the source representation of a spread-out moment tensor. Note however, in this context, that our source location favourably coincides with a GLL point, resulting in higher accuracy than freely chosen (ξ, η) (Deville *et al.* 2002).

5.3 Global wave propagation

After validating the stiffness terms and source terms, respectively, we now take on full global wave propagation. The moment-tensor source with magnitude $M_0 = 10^{20}$ Nm is located at a depth of $r_s = 344$ km, the unity single force is applied at the surface $r_r = r_0$ and the respective source time functions are Dirac delta functions. We record seismic displacement along the surface within the $\phi = 0$ plane at epicentral distances $7.5^\circ \leq \theta_{\mathrm{rec}} \leq 180^\circ$, separated by 7.5°, using the mesh in Fig. 1 and polynomial order $N = 5$. The time step is $\Delta t = 0.25$ s leading to a Courant number $\mathcal{C} = 0.37$, and seismogram length $t_{\max} = 8000$ s. We convolve the Green functions with a Ricker wavelet (first derivative of a Gaussian as defined in Section 5.2) of dominant period $T_0 = 100$ s. The number of grid points per wavelength is $n_\lambda = vT_0/h$, where v is the seismic velocity and h is the grid spacing. For the mesh and parameter choice in this section, the dominant frequencies of an S wave are sampled by $8 \leq n_\lambda \leq 85$ grid points, depending on the location within the mesh. Note that maximal frequencies of the source time functions are about two times higher than dominant frequencies, such that n_λ is in accordance with heuristic choices in 3-D SEM simulations (e.g. Komatitsch & Tromp 2002a). We remain at relatively low frequencies in this test case since the SEM is scalable and the critical parameter, the number of points per wavelength, is independent of the period. Our meshes are automatically adapted to these numerical parameters accordingly and as such, absolute frequencies do not intrinsically determine accuracy interpretations. Rather than describing additional issues resulting from high frequencies such as parallelization or computation time, our objective here is to delineate the accuracy of the whole wavefield penetrating the sphere for all source types. All SEM-based seismograms are compared to synthetics from normal-mode summation, using a mode catalogue

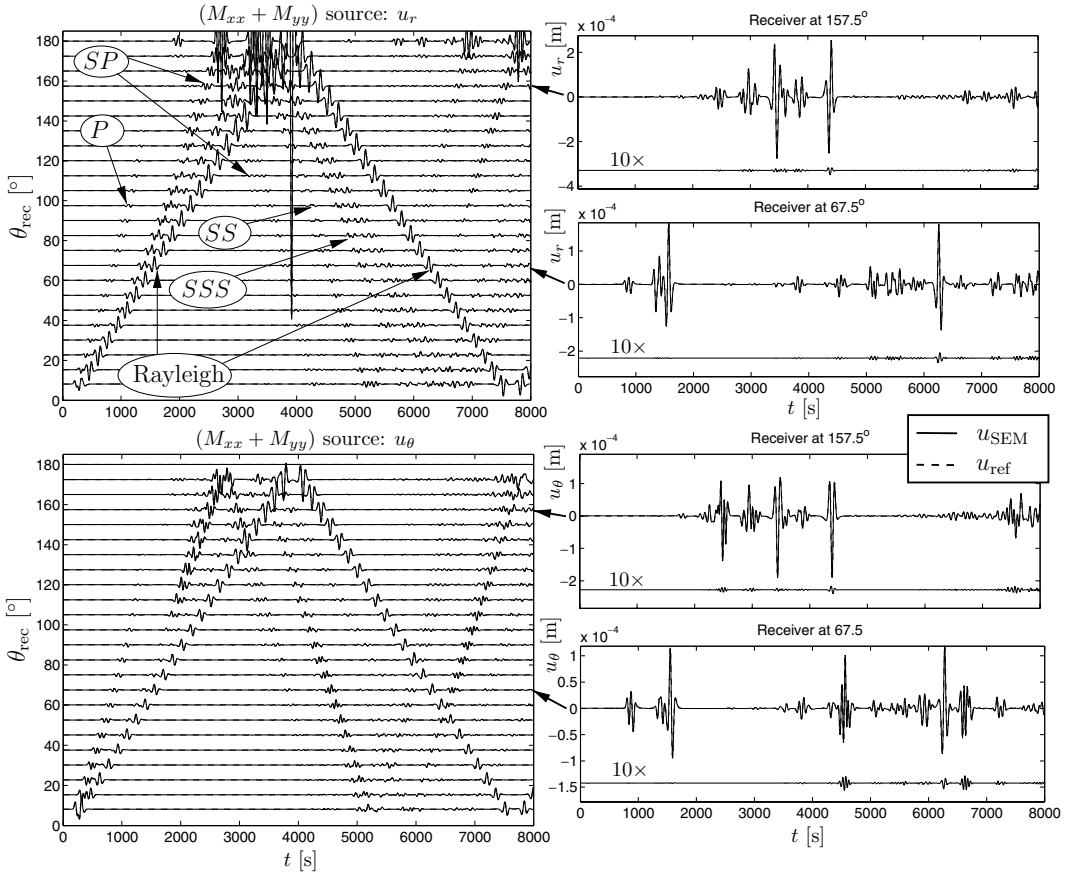

Figure 6. Global wave propagation upon an $(M_{xx} + M_{yy})$ monopole source located at 344 km depth. The top (bottom) left panel depicts the r (θ) component of both SEM-based (solid lines) and normal-mode displacements (dashed lines) along the surface in the $\phi = 0$ plane for a dominant period of $T_0 = 100$ s. The amplitudes have been scaled with a factor of ${\theta_{\rm rec}}^{1/3}$ to identify most phases at all distances. Some prominent direct, multiple and surface wave phases are labelled in the top left figure. The panels on the right depict two sample traces from the sections on the left for both SEM (solid lines) and normal-mode simulations (thicker, dashed lines) in absolute displacement values. Below each seismogram is the residual waveform between SEM and normal-mode trace, magnified by a factor of 10. Note the different absolute displacement scales for each of the single trace panels.

up to 45 mHz. In Figs 6–9, we show seismograms for each of the respective source types and varying displacement components. For brevity, we only show one moment-tensor source of each multipole type and one point-force source, i.e. four different cases. We chose excitation types for which the ϕ component vanishes at $\phi = 0$, i.e. only show r and θ components of the displacement. All traces in the global sections are scaled by the same, but distance-dependent factor of ${\theta_{\rm rec}}^{1/3}$ to maintain a visible amplitude for most phases at all distances. For orientation, the predominant phase reaching the antipode at 3900 s is the Rayleigh wave. The fit between the SEM (solid lines) and normal-mode summation (dashed lines) is very good for all source types, phases, and distances, inasmuch as the two traces are indistinguishable for all global sections. Also note that we correctly obtain the large amplitudes on the last trace at 180° (e.g. Fig. 6 top left) for all phases, in particular those that meet at the antipode, such as surface waves and multiples. For each type and component, we show two sample traces at distances 67.5° and 157.5°, in which we can verify the excellent fits of all phases. A magnified residual waveform, defined as $\Delta u = 10 \times (u_{\rm ref} - u_{\rm SEM})$ for any of the components, is shown below each of the single traces to underscore the notion that for all cases we observe very small residuals of comparable size for all distances, seismic phases, and source types. The accuracy is of the same order of magnitude as other SEM-based wave-propagation algorithms, for example, in 3-D. We quantify the residual in an $\mathbb{L}^2$ sense similar to the static case (eq. 45), but averaged over time for a given receiver at epicentral distance $\theta_{\rm rec}$, as

$$\ell_{\rm time}(\theta_{\rm rec}) = \left\{ \frac{\int_0^{t_{\rm max}} [u_{\rm ref}(\theta_{\rm rec}, t) - u_{\rm SEM}(\theta_{\rm rec}, t)]^2 \, dt}{\int_0^{t_{\rm max}} [u_{\rm ref}(\theta_{\rm rec}, t)]^2 \, dt} \right\}^{1/2}, \tag{47}$$

which is shown in Fig. 10 for the r and θ components corresponding to the four simulations of Figs 6–9. We plot $\ell_{\rm time}$ as a function of epicentral distances $15° \leq \theta_{\rm rec} \leq 180°$ only, since closer traces are subject to faulty source ghost phases appearing in the mode summation and should hence be ignored for detailed accuracy studies, especially after our validation of the accuracy in the source vicinity in the last section. The effect can still be observed in slightly larger residuals at 7.5° which result from these erroneous phases. The first key observation in Fig. 10 is the apparent independence of epicentral distance and, consequently, lack of numerical dispersion, which is important for our ultimate purpose of storing global wavefields. One should, however, bear in mind that we employ a second-order time extrapolation scheme

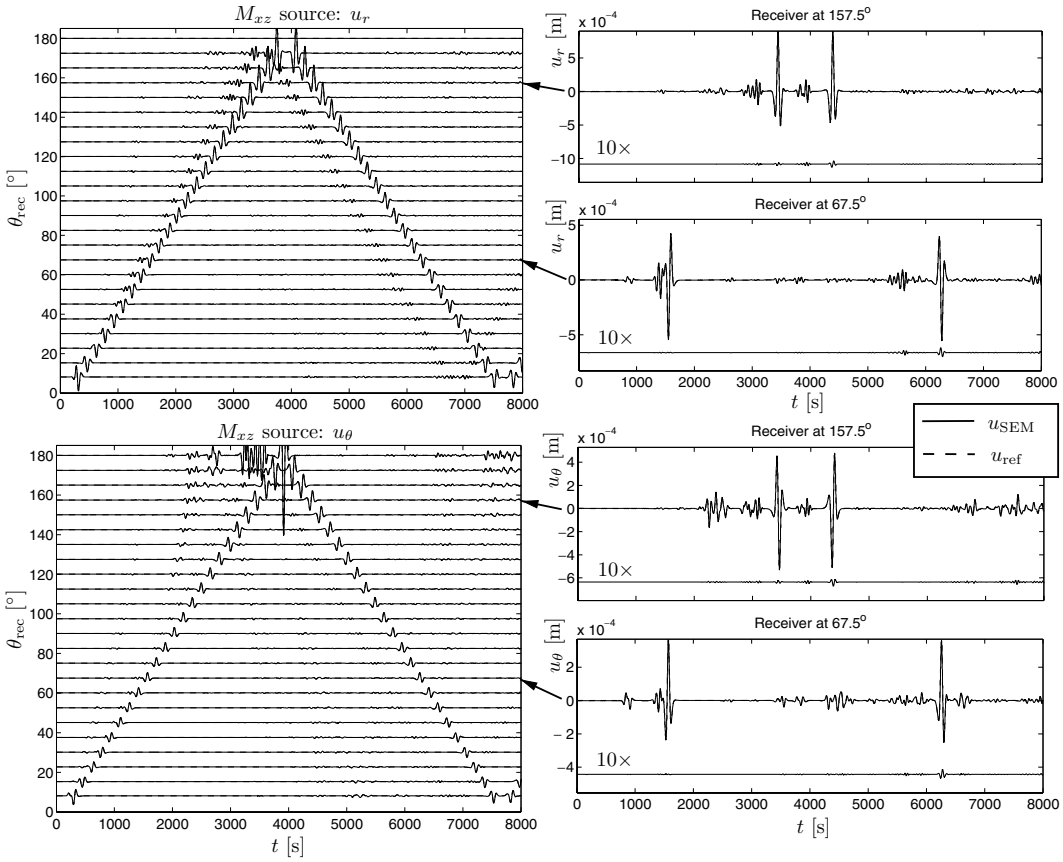

Figure 7. Global wave propagation upon an M_{xz} dipole source located at 344 km depth. See Fig. 6 for further details.

whose dispersive error is simply buried within our acceptable thresholds, mainly due to the restrictive small time step as constrained by eq. (23). Secondly, the $\mathbb{L}^2$ residuals are of similar magnitude for all excitation types and both components, again an important consideration for accurately representing the full moment tensor and receiver components. The $\mathbb{L}^2$ residual is consistently between 0.5 and 1 per cent, which supports our previous assertion that full-wave propagation is prone to significantly larger $\mathbb{L}^2$ residuals than the static case, but still very favourable compared to other wave propagation methods such as FD which often have squared $\mathbb{L}^2$ norms ('energy misfit') around 1 per cent in similar settings (e.g. Igel *et al.* 2002), that is, more than 10 times higher than our results in Fig. 10. One should, however, exercise caution to generalize these comparisons, since the specific accuracy depends on a variety of parameters such as polynomial order, dimensionality, mesh topology and extent of distortion, background model, or number of points per wavelength. The mildly higher residuals for the vertical single force at $\leq 60^\circ$ stem from the fact that the source is located at the surface and hence generates, relative to other phases, larger surface waves at small distances, in addition to the abundance of erroneous ghost phases in the mode summation, as evidenced by residual amplitudes at 150 s in Fig. 9. The dipole simulations (Fig. 7) show a slightly smaller residual compared to other excitation types due to the lack of significant high-frequency multiples which dominate the accuracy in other cases (e.g. Fig. 6, at 4500 s on the bottom right panel showing the θ component at distance 67.5°). These high-frequency arrivals are naturally the most critical and least accurate fractions of a seismogram.

5.4 Energy conservation

Examining the energy conservation of the numerical scheme is a simple check on the consistency especially of the temporal discretization. In fact, the explicit Newmark scheme used here (eq. 22) does not specifically conserve energy, but the resultant total energy is expected to exhibit a bounded fluctuation (e.g. Kane *et al.* 2000; Hughes 1987). The total energy following excitation by a source is $E_{\rm tot} = E_{\rm kin} + E_{\rm pot}$, where the kinetic energy at time t is given by

$$E_{\rm kin}(t) = \frac{1}{2}\int_{\oplus} \rho\,[\partial_t \mathbf{u}(t)]^2\; d^3\mathbf{r} \approx \frac{1}{2}\dot{\mathbf{u}}^{\rm T}(t)\mathbf{M}\dot{\mathbf{u}}(t), \tag{48}$$

and the stored, potential or elastic energy in an isotropic earth at time t is

$$E_{\rm pot}(t) = \frac{1}{2}\int_{\oplus} \left\{\lambda\,[\boldsymbol{\nabla}\cdot\mathbf{u}(t)]^2 + \mu\boldsymbol{\nabla}\mathbf{u}(t) : \left[\boldsymbol{\nabla}\mathbf{u}(t) + (\boldsymbol{\nabla}\mathbf{u}(t))^{\rm T}\right]\right\} d^3\mathbf{r} \approx \frac{1}{2}\mathbf{u}^{\rm T}(t)\mathbf{K}\mathbf{u}(t). \tag{49}$$

Fig. 11 shows the kinetic, potential and half of the total energy calculated at every 10th time step for the simulations in Section 5.3. The time window chosen includes the case of kinetic and potential energy reaching respective extrema when *SS* and higher multiples (between 3200

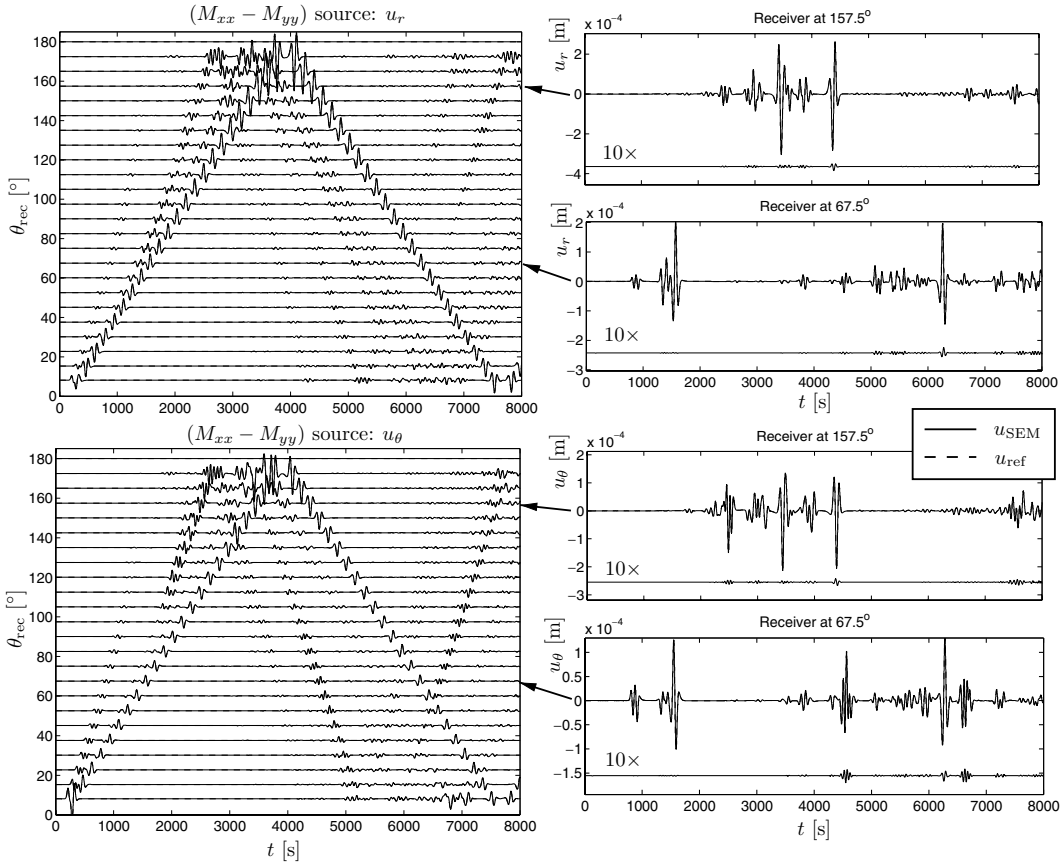

Figure 8. Global wave propagation upon an $(M_{xx} - M_{yy})$ quadrupole source located at 344 km depth. See Fig. 6 for further details.

and 3500 s) or globe-encircling surface waves (at 3900 s) pass through the antipode. The total energy, indicated by the bold straight line, is constant over time for all cases. Note the differing magnitude for each of the excitation systems. We conclude that the time evolution scheme we employ does not dissipate or show any non-conserving behaviour throughout any of the simulations. Additionally, the energy conservation indicates the fact that the approach is based upon a fully (3-D) enclosed system without artificial boundaries; for example, the masking for axial boundary conditions is indeed 'essential' and not absorbing or damping.

6 CONCLUSIONS

This paper introduces a spectral-element method to solve the 3-D forward wave-propagation problem of spherically symmetric earth models as a source-decomposed, equivalent system of six 2-D problems. Axial elements are treated using a different quadrature compared to non-axial elements to accommodate the axial boundary conditions. The resultant system consists of three weak systems for monopole, dipole, and quadrupole excitation types. The implementation of the method is thoroughly benchmarked for specific settings emulating the different terms of the discrete system. The mass and stiffness terms are validated using toroidal eigenfunctions to solve the elastostatic wave equation in a homogeneous solid sphere. These eigenfunctions allow for an easily implemented solution at each grid point, hence highlighting differences in accuracy depending upon local mesh properties such as the vicinity of coarsening levels, the axis or the free surface. By varying degree n and overtone l, we obtain a handle on the resolution capacity of a given mesh. Quantitatively, we compute the $\mathbb{L}^2$ norm of the residual to demonstrate the spectral convergence as a function of the polynomial order for both dipole and quadrupole types. The remaining source term is analysed by studying the near-source radiation upon an explosion, verified using exact analytical expressions. We observe partly significant misfits in the elements bearing non-zero source vectors in the spread-out moment-tensor formulation for the SEM, which disappear when recording the wavefield at least two elements away from the actual physical source location, leading to highly accurate displacement traces. Global wave propagation in a homogeneous solid sphere is validated against normal-mode summation for all source types and again reveals an excellent fit for all spatial and temporal points. The accuracy is furthermore independent of distance, time, and source type. The lack of dispersion for the overall wavefield is merely a consequence of the spatially spectral accuracy and a time step chosen sufficiently small such that the temporal error does not hamper the overall accuracy. For instance, if we considered the $\mathbb{L}^2$ norm of a singular phase only, we expect a linear increase in error with distance which is, however, still negligible due to the small time step. Higher-order extrapolation schemes may be considered in the future to further reduce dispersion. Finally, the total energy of the numerical scheme is conserved for all source types, indicating a consistent time-stepping algorithm as well as an enclosed domain with proper boundary treatment. At large, this approach is a

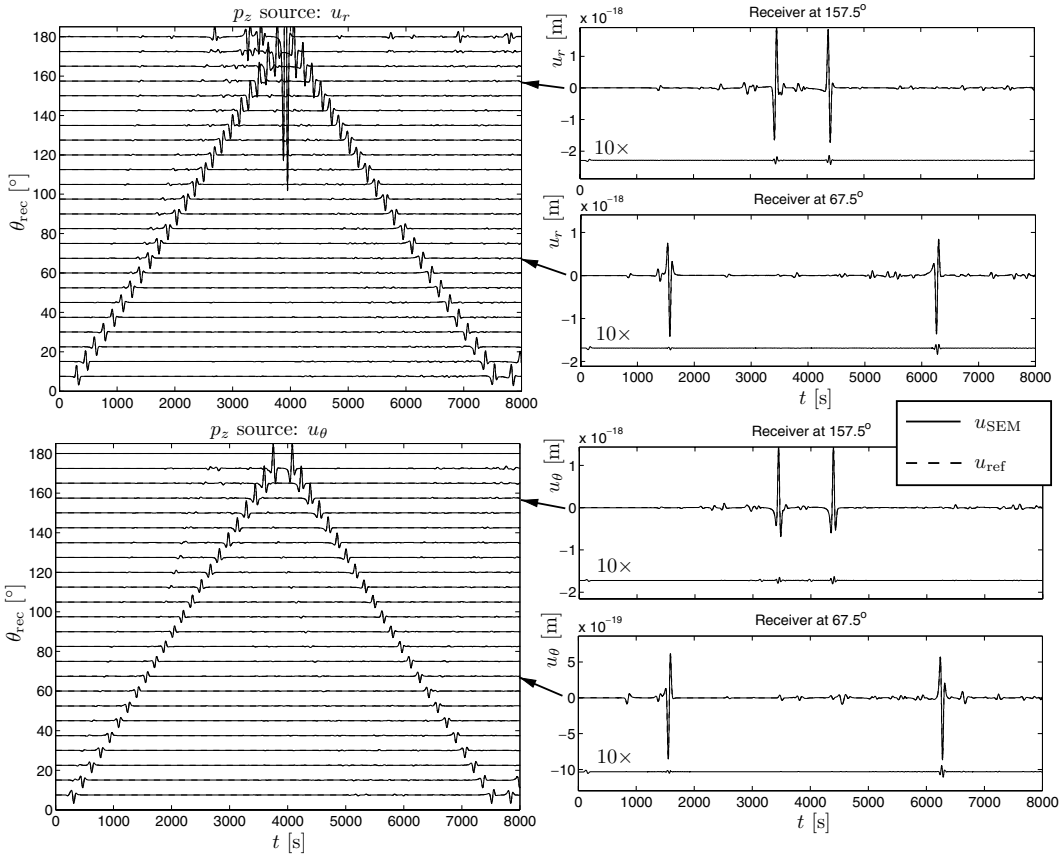

Figure 9. Global wave propagation upon a p_z vertical single force located at the surface ('Lamb's Problem'). Note the small absolute amplitudes on the single traces as a result of applying a unit force of 1 N as the source. In the residual traces, amplitudes at 150 s represent the so-called source ghost, an erroneous phase within the normal-mode summation. See Fig. 6 for other details.

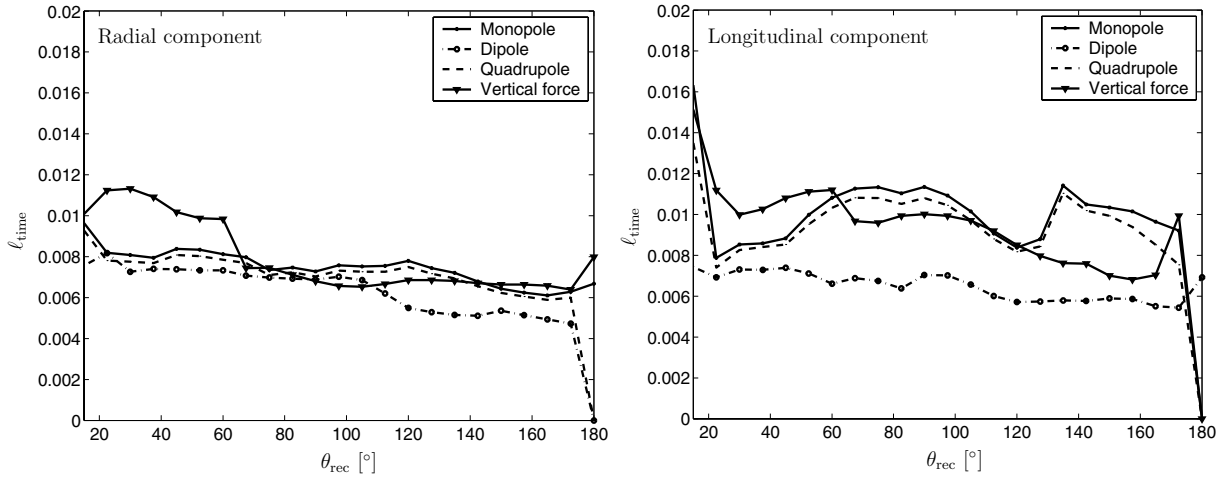

Figure 10. Time-averaged $\mathbb{L}^2$ norm $\ell_{\rm time}$ of each trace as a function of epicentral distance for all source types. Left: radial component; right: longitudinal component.

novel and fully functional method for including seismic moment tensors in a 2-D computational domain while retaining the 3-D wavefield properties. This stage of verifying the 3-D to 2-D reduction for all source types represents the crucial accomplishment towards eventually computing full Fréchet sensitivity kernels. Clearly, the extension to earth-like background models such as PREM (Dziewonski & Anderson 1981) is the subject of ongoing work, to appear in a subsequent paper.

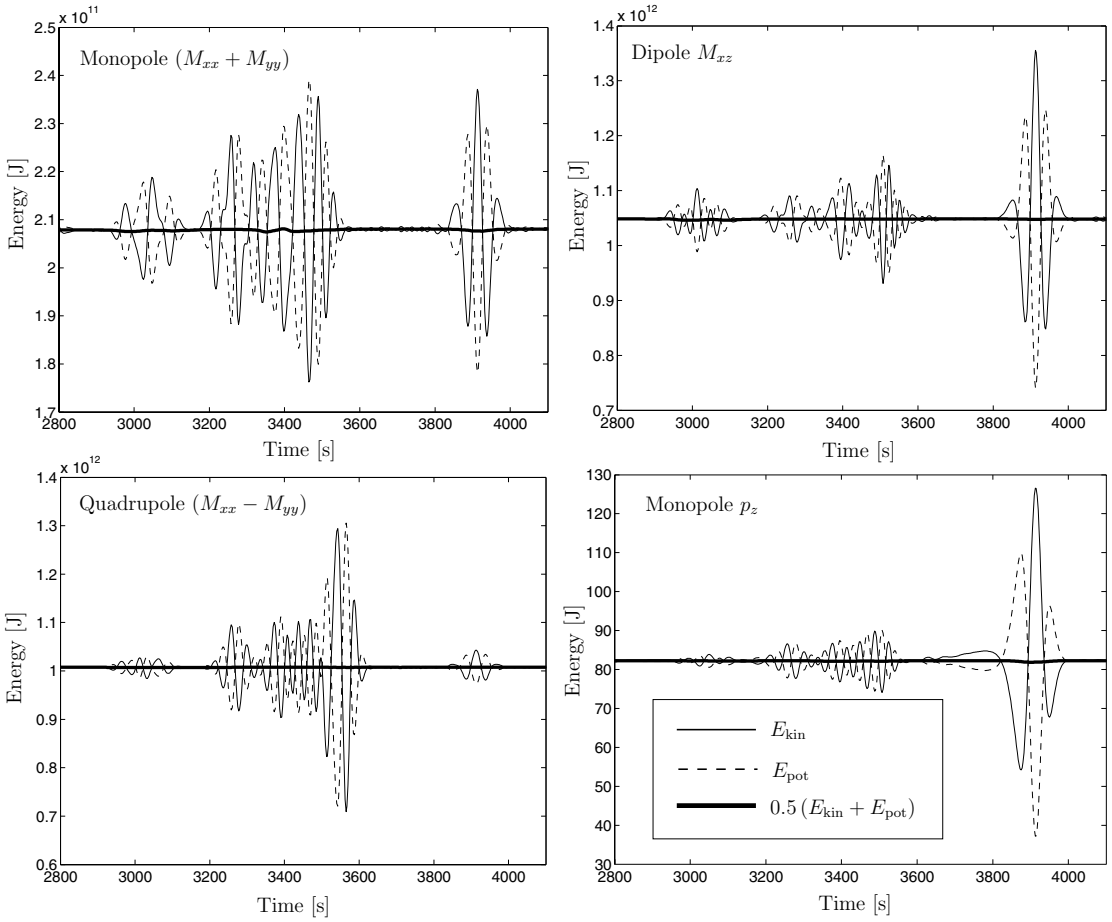

Figure 11. Energy conservation for the monopole (moment tensor and single force), dipole, and quadrupole simulations in Section 5.3. Kinetic (eq. 48) and potential energy (eq. 49) add up to the total energy (bold straight lines) to be conserved. The time window shown here includes some of the instances during which kinetic and potential energies differ maximally when, for example, *S* multiples (at 3200–3500 s) or Rayleigh waves (at 3900 s) meet at the antipode.

ACKNOWLEDGMENTS

We are grateful to Yann Capdeville and Emmanuel Chaljub for providing us with the normal-mode algorithms and insightful discussions about the SEM, to Dimitri Komatitsch and Jeroen Tromp for allowing us to use their 3-D SEM code, and to Guust Nolet for discussions. Constructive comments by Jeroen Tromp, an anonymous reviewer, *GJI* editor Yanick Ricard and Jean-Paul Ampuero greatly improved the manuscript. TN-M would like to thank the Institut de Physique du Globe de Paris and the Laboratoire de Géophysique Interne et Tectonophysique in Grenoble for their hospitality during his stays there. Financial support for this work has been provided by the U. S. National Science Foundation under Grants EAR-0105387 and EAR-0113050.

REFERENCES

Bao, H., Bielak, J., Ghattas, O., Kallivokas, L.F., O'Hallaron, D.R., Shewchuk, J.R. & Xu, J., 1998. Large-scale simulation of elastic wave propagation in heterogeneous media on parallel computers, *Comput. Methods Appl. Mech. Eng.,* **152,** 85–102.

Bernardi, C., Dauge, M. & Maday, Y., 1999. *Spectral Methods for Axisymmetric Domains*, Vol. 3 of Series in Applied Mathematics, Gauthier-Villars, Paris, Numerical algorithms and tests by Mejdi Azaïez.

Chaljub, E., 2000. Modélisation numérique de la propagation d'ondes sismiques en géométrie sphérique: application à la sismologie globale, *PhD thesis*, Université de Paris 7, France.

Chaljub, E. & Tarantola, A., 1997. Sensitivity of SS precursors to topography on the upper-mantle 660 km discontinuity, *Geophys. Res. Lett.,* **24,** 2613–2616.

Chaljub, E. & Valette, B., 2004. Spectral element modeling of three dimensional wave propagation in a self-gravitating Earth with an arbitrarily stratified outer core, *Geophys. J. Int.,* **158,** 131–141.

Chaljub, E., Capdeville, Y. & Vilotte, J.-P., 2003. Solving elastodynamics in a fluid-solid heterogeneous sphere: a parallel spectral element approximation on non-conforming grids, *J. Comp. Phys.,* **187,** 457–491.

Chaljub, E., Komatitsch, D., Vilotte, J.P., Capdeville, Y., Valette, B. & Festa, G., 2006. Spectral-element analysis in seismology, in *Advances in Wave Propagation in Heterogeneous Media*, eds Wu, R. & Maupin, V., Advances in Geophysics, Elsevier, in press.

Cummins, P., Geller, R., Hatori, T. & Takeuchi, N., 1994a. DSM complete synthetic seismograms: SH, spherically symmetric, case, *Geophys. Res. Lett.,* **21,** 533–536.

Cummins, P., Geller, R. & Takeuchi, N., 1994b. DSM complete synthetic seismograms: P-SV, spherically symmetric, case, *Geophys. Res. Lett.,* **21,** 1663–1666.

Dahlen, F.A. & Tromp, J., 1998. *Theoretical Global Seismology*, Princeton University Press, Princeton, New Jersey.

Deville, M.O., Fischer, P.F. & Mund, E.H., 2002. *High-Order Methods for Incompressible Fluid Flow*, Vol. 2 of Cambridge monographs on applied and computational mathematics, Cambridge University Press, Cambridge.

Dziewonski, A.M. & Anderson, D.L., 1981. Preliminary Reference Earth Model, *Phys. Earth planet. Inter.,* **25,** 297–356.

Faccioli, E., Maggio, F., Paolucci, R. & Quarteroni, A., 1997. 2D and 3D elastic wave propagation by a pseudo-spectral domain decomposition method, *J. Seismol.,* **1,** 237–251.

Fournier, A., 2004. Incompressible Fluid Flows in Rapidly Rotating Cavities, *PhD thesis*, Princeton University, New Jersey.

Fournier, A., Bunge, H.-P., Hollerbach, R. & Vilotte, J.-P., 2004. Application of the spectral element method to the axisymmetric Navier-Stokes equation, *Geophys. J. Int.,* **156,** 682–700.

Fournier, A., Bunge, H.-P., Hollerbach, R. & Vilotte, J.-P., 2005. A Fourier-spectral element algorithm for thermal convection in rotating axisymmetric containers, *J. Comp. Phys.,* **204,** 462–489.

Friederich, W. & Dalkolmo, J., 1995. Complete synthetic seismograms for a spherically symmetric Earth by a numerical computation of the Green's function in the frequency domain, *Geophys. J. Int.,* **122,** 537–550.

Furumura, T., Kennett, B.L. N. & Furumura, M., 1998. Seismic wavefield calculation for laterally heterogeneous whole Earth models using the pseudospectral method, *Geophys. J. Int.,* **135,** 845–860.

Geller, R.J. & Ohminato, T., 1994. Computation of synthetic seismograms and their partial derivatives for heterogeneous media with arbitrary natural boundary conditions using the direct solution method, *Geophys. J. Int.,* **116,** 421–446.

Geller, R. & Takeuchi, N., 1998. Optimally accurate time domain finite difference scheme for the elastic wave equation: one-dimensional case, *Geophys. J. Int.,* **135,** 48–62.

Hughes, T.J.R., 1987. *The Finite Element Method: Linear Static and Dynamic Finite Element Analysis*, Prentice Hall, Englewood Cliffs, New Jersey.

Igel, H. & Weber, M., 1995. SH-wave propagation in the whole mantle using high-order finite differences, *Geophys. Res. Lett.,* **22,** 731–734.

Igel, H. & Weber, M., 1996. P-SV wave propagation in the Earth's mantle using finite differences: application to heterogeneous lowermost mantle structure, *Geophys. Res. Lett.,* **23,** 415–418.

Igel, H., Nissen-Meyer, T. & Jahnke, G., 2002. Wave propagation in 3D spherical sections: Effects of subduction zones, *Phys. Earth planet. Inter.,* **132,** 219–234.

Kane, C., Marsden, J.E., Ortiz, M. & West, M., 2000. Variational integrators and the Newmark algorithm for conservative and dissipative mechanical systems, *Int. J. Numer. Meth. Eng.,* **49,** 1295–1325.

Karniadakis, G.E. & Sherwin, S.J., 1999. *Spectral/hp Element Methods for CFD*, Oxford University Press, Oxford.

Käser, M. & Dumbser, M., 2006. An arbitrary high-order discontinuous Galerkin method for elastic waves on unstructures meshes – I. The two-dimensional isotropic case with external source terms, *Geophys. J. Int.,* **166,** 855–877.

Kawai, K., Takeuchi, N. & Geller, R.J., 2006. Complete synthetic seismograms up to 2 hz for transversely isotropic spherically symmetric media, *Geophys. J. Int.,* **164,** 411–424.

Komatitsch, D. & Tromp, J., 1999. Introduction to the spectral-element method for 3-D seismic wave propagation, *Geophys. J. Int.,* **139,** 806–822.

Komatitsch, D. & Tromp, J., 2002b. Spectral-element simulations of global seismic wave propagation—II. 3-D models, oceans, rotation, and self-gravitation, *Geophys. J. Int.,* **150,** 303–318.

Komatitsch, D. & Vilotte, J.P., 1998. The spectral-element method: an efficient tool to simulate the seismic response of 2D and 3D geological structures, *Bull. seism. Soc. Am.,* **88,** 368–392.

Komatitsch, D. & Tromp, J., 2002a. Spectral-element simulations of global seismic wave propagation—I. Validation, *Geophys. J. Int.,* **149,** 390–412.

Komatitsch, D., Tsuboi, S., Chen, J. & Tromp, J., 2003. A 14.6 billion degrees of freedom, 5 teraflop, 2.5 terabyte earthquake simulation on the Earth Simulator, *Proceedings of the ACM/IEEE Supercomputing SC'2003 conference*, on CD-ROM.

Lognonné, P. & Romanowicz, B., 1990. Modeling of coupled normal modes of the Earth: The spectral method, *Geophys. J. Int.,* **102,** 365–395.

Mizutani, H., Geller, R. & Takeuchi, N., 2000. Comparison of accuracy and efficiency of time-domain schemes for calculating synthetic seismograms, *Phys. Earth planet. Inter.,* **119,** 75–97.

Nissen-Meyer, T., Dahlen, F.A. & Fournier, A., 2007. Spherical-earth Fréchet sensitivity kernels, *Geophys. J. Int.,* doi:10.1111/j.1365-246X.2006.03123.x.

Robertsson, J.O.A., 1996. A numerical free-surface condition for elastic/viscoelastic finite-difference modeling in the presence of topography, *Geophysics,* **61,** 1921–1934.

Schuberth, B., 2003. The spectral element method for seismic wave propagation: Theory, implementation and comparison to Finite Difference Methods, *Master's thesis*, Ludwig-Maximilians-Universität München, unpublished.

Seriani, G., 1998. 3-D large-scale wave propagation modeling by a spectral element method on a Cray T3E multiprocessor, *Comput. Meth. Appl. Mech. Eng.,* **164,** 235–247.

Takeuchi, N., Geller, R. & Cummins, P., 2000. Complete synthetic seismograms for 3-D heterogeneous Earth models computed using modifed DSM operators and their applicability to inversion for Earth structure, *Phys. Earth planet. Inter.,* **119,** 25–36.

Thomas, C., Igel, H., Weber, M. & Scherbaum, F., 2000. Acoustic simulation of P-wave propagation in a heterogeneous spherical earth: numerical method and application to precursor energy to PKPdf, *Geophys. J. Int.,* **141,** 307–320.

Toyokuni, G., Takenaka, H., Wang, Y. & Kennett, B.L.N., 2005. Quasi-spherical approach for seismic wave modeling in a 2D slice of a global Earth model with lateral heterogeneity, *Geophys. Res. Lett.,* **32,** doi:10.1029/2004GL022180.

Tsuboi, S., Komatitsch, D., Chen, J. & Tromp, J., 2003. Broadband simulation of the 2002 Denali, Alaska, Mw = 7.9 earthquake on the Earth Simulator, *Phys. Earth planet. Inter.,* **139,** 305–313.

Zhang, S. & Jin, J.M., 1996. *Computation of Special Functions*, John Wiley & Sons, New York, routines available at http://jin.ece.uiuc.edu/routines/routines.html.

APPENDIX A: SPECTRAL-ELEMENT LIBRARY

In the interest of completeness, we list all relevant mathematical foundations underlying the SEM as used here, without proofs or further explanation. For details, see Hughes (1987) and Karniadakis & Sherwin (1999) on the general finite element method including geometrical mapping, Komatitsch & Tromp (1999) on the elastodynamic spectral-element method, Bernardi *et al.* (1999); Fournier *et al.* (2004); Fournier (2004) on axisymmetric spectral elements, and Deville *et al.* (2002) on tensor products and global numbering.

A1 Geometrical mapping

Depending on the geometrical complexity of elements, we employ either analytical or subparametric mapping between the reference system (ξ, η) and the physical coordinates $\mathbf{x} = (s, z)$ (Fournier *et al.* 2004). We distinguish three fundamental elemental geometries as depicted in Fig. A1. Given the set of vertex coordinates $\{\mathbf{x}_1, \mathbf{x}_3, \mathbf{x}_5, \mathbf{x}_7\}$ for the most common, circular type (A) and the circular-linear transition type (C), any (s, z) corresponding to reference coordinates (ξ, η) is computed by analytical transformation formulae for the $z \geq 0$

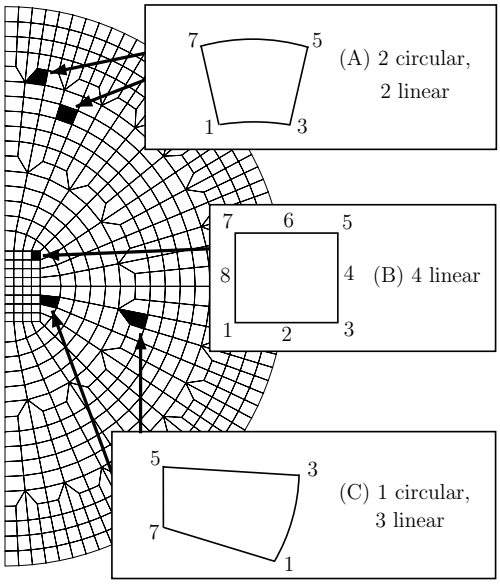

Figure A1. Elemental shapes. Sketch illustrating the three fundamental element-shape geometries used to construct the mesh. The mesh on the left is a low-resolution example to simply highlight the skeleton. (A) is the analytically expressed circular element shape, (B) is the purely rectangular element shape necessary to mesh the central part of the domain and computed in a subparametric fashion (serendipity quadrilateral), and (C) is the connecting type between (A) and (B), mapped using an analytical formula similar to type (A). Both (A) and (C) take on two different shapes, one of which is located within the coarsening region, respectively. Numbers denote the collocation point indices as used in Appendix A1.

hemisphere

$$s(\xi,\eta) = \tfrac{1}{2}\left[(1-\eta)\,\tilde{s}_{\rm bot}(\xi) + (1+\eta)\,\tilde{s}_{\rm top}(\xi)\right],\ z(\xi,\eta) = \tfrac{1}{2}\left[(1-\eta)\,\tilde{z}_{\rm bot}(\xi) + (1+\eta)\,\tilde{z}_{\rm top}(\xi)\right], \tag{A1}$$

where $\{\tilde{s},\tilde{z}\}_{\rm top}$ are the same for both types:

$$\tilde{s}_{\rm top}(\xi) = r_7 \sin\left\{\tfrac{1}{2}\left[(1-\xi)\,\theta_7 + (1+\xi)\,\theta_5\right]\right\},\ \tilde{z}_{\rm top}(\xi) = r_7 \cos\left\{\tfrac{1}{2}\left[(1-\xi)\,\theta_7 + (1+\xi)\,\theta_5\right]\right\}. \tag{A2}$$

$\{\tilde{s},\tilde{z}\}_{\rm bot}$ for type (A) read

$$\tilde{s}_{\rm bot}(\xi) = r_1 \sin\left\{\tfrac{1}{2}\left[(1-\xi)\,\theta_1 + (1+\xi)\,\theta_3\right]\right\},\ \tilde{z}_{\rm bot}(\xi) = r_1 \cos\left\{\tfrac{1}{2}\left[(1-\xi)\,\theta_1 + (1+\xi)\,\theta_3\right]\right\}, \tag{A3}$$

and for type (C)

$$\tilde{s}_{\rm bot}(\xi) = \tfrac{1}{2} r_1\left[(1-\xi)\sin\theta_1 + (1+\xi)\sin\theta_3\right],\ \tilde{z}_{\rm bot} = \tfrac{1}{2} r_1\left[(1-\xi)\cos\theta_1 + (1+\xi)\cos\theta_3\right]. \tag{A4}$$

For $z < 0$, the mesh is mirrored by swapping the respective vertices $\mathbf{x}_1 \longleftrightarrow \mathbf{x}_7$ and $\mathbf{x}_3 \longleftrightarrow \mathbf{x}_5$ in the above formulae. The linear element type (B) is parametrized via eight control nodes as shown in Fig. A1. We approximate the mapping by (e.g. Komatitsch & Tromp 1999)

$$\mathbf{x}(\xi,\eta) = \sum_{a=1}^{n_a} N_a(\xi,\eta)\mathbf{x}_a,\ \text{and derivatives as}\ \ \frac{d\mathbf{x}(\xi,\eta)}{d(\xi,\eta)} = \sum_{a=1}^{n_a} \frac{dN_a(\xi,\eta)}{d(\xi,\eta)}\mathbf{x}_a, \tag{A5}$$

where N_a are shape functions defining the geometry anchored at the $n_a = 8$ control points $\mathbf{x}_a$, which define the so-called serendipity quadrilateral (Hughes 1987). The shape functions are given by

$$N_1(\xi,\eta) = (1-\xi)(1-\eta)(-1-\xi-\eta)/4, \tag{A6}$$

$$N_2(\xi,\eta) = (1-\xi^2)(1-\eta)/2, \tag{A7}$$

$$N_3(\xi,\eta) = (1+\xi)(1-\eta)(-1+\xi-\eta)/4, \tag{A8}$$

$$N_4(\xi,\eta) = (1+\xi)(1-\eta^2)/2, \tag{A9}$$

$$N_5(\xi,\eta) = (1+\xi)(1+\eta)(-1+\xi+\eta)/4, \tag{A10}$$

$$N_6(\xi,\eta) = (1-\xi^2)(1+\eta)/2, \tag{A11}$$

$$N_7(\xi,\eta) = (1-\xi)(1+\eta)(-1-\xi+\eta)/4, \tag{A12}$$

$$N_8(\xi,\eta) = (1-\xi)(1-\eta^2)/2. \tag{A13}$$

Table A1. Definitions of tensor notations and product operations, based on definitions in Table 1.

Type	Matrix notation	Index notation	Axial vector notation	Axial index notation
Pre-computed tensor	${}_\epsilon\mathbf{B}_{s_\xi}$	${}_\epsilon B^{ij}_{s_\xi}$	${}_\epsilon\mathbf{B}^0_{s_\xi}$	${}_\epsilon B^{0j}_{s_\xi}$
Derivative tensor ξ	$\mathbf{D}_\xi$	D^{Ii}_ξ	$\mathbf{D}^0_\xi$	D^{I0}_ξ
Transpose of $\mathbf{D}_\xi$	$\mathbf{D}^{\mathrm{T}}_\xi$	D^{iI}_ξ	$(\mathbf{D}^0_\xi)^{\mathrm{T}}$	D^{i0}_ξ
Derivative tensor η	$\mathbf{D}_\eta$	D^{iJ}_η		
Matrix product	$\mathbf{X} = \mathbf{u} \otimes \mathbf{D}_\eta$	$X^{IJ} = \sum_j u^{Ij} D^{jJ}_\eta$	$\mathbf{X}^0 = \mathbf{u}^0 \otimes \mathbf{D}_\eta$	$X^{0J} = \sum_j u^{0j} D^{jJ}_\eta$
Hadamard product	$\mathbf{X} = \mathbf{A} \odot \mathbf{u}$	$X^{IJ} = A^{IJ} u^{IJ}$	$\mathbf{X}^0 = {}_\epsilon\mathbf{B}^0_{s_\xi} \odot \mathbf{u}^0$	$X^{0j} = {}_\epsilon B^{0j}_{z_\eta} u^{0j}$
Dyadic product			$\mathbf{X} = \mathbf{D}^0_\xi\, \mathbf{u}^0$	$X^{IJ} = D^{I0}_\xi\, u^{0J}$

Given the coordinates $\mathbf{x}_a$ at the eight control nodes, one may then readily compute coordinates at any point $\mathbf{x}\,(\xi, \eta)$, particularly the grid points used in the quadrature, as defined in the following section. Partial derivatives $\partial\mathbf{x}/\partial(\xi, \eta)$ and the Jacobian $\mathcal{J} = \partial_\xi s \partial_\eta z - \partial_\xi z \partial_\eta s$ are obtained by straightforward differentiation of eqs (A1)–(A13).

A2 Gauss-Lobatto–Legendre quadrature

The solution to the differential equation

$$\partial_\xi[(1-\xi^2)\partial_\xi P_N] = -N\,(N+1)\,P_N \tag{A14}$$

with $P_N(1) = 1$ and $P_N(-1) = (-1)^N$ is a Legendre polynomial P_N of order N

$$P_N(\xi) = \frac{1}{2^N N!}\frac{d^N}{d\xi^N}(\xi^2-1)^N \tag{A15}$$

which may be computed using the induction formula

$$P_N(\xi) = \frac{1}{N}\left[(2N-1)\xi\,P_{N-1}(\xi) - (N-1)P_{N-2}(\xi)\right],\ P_0(\xi) = 1,\ P_1(\xi) = \xi. \tag{A16}$$

Legendre Polynomials are orthogonal in $\mathbb{L}^2$:

$$\int_{-1}^{1} P_{N_1}(\xi)P_{N_2}(\xi)\,d\xi = \begin{cases} 0, & (N_1 \neq N_2), \\ 1/(N_1+1/2), & (N_1 = N_2). \end{cases} \tag{A17}$$

We utilize Gauss–Lobatto–Legendre nodes as quadrature points $\xi^N_i, 0 \le i \le N$ as the zeroes of $(1-\xi^2)\partial_\xi P_N(\xi)$. Gauss-Lobatto–Legendre quadrature weights σ^N_i for non-axial elements are given by

$$\sigma^N_i = \frac{2}{N(N+1)[P_N(\xi^N_i)]^2} \tag{A18}$$

and the corresponding basis functions, the Lagrange interpolating functions $l^N_i(\xi)$, may be calculated via

$$l^N_i(\xi) = \begin{cases} (-1)^N \frac{(1-\xi)P'_N(\xi)}{N(N+1)}, & i = 0, \\ \frac{1}{N(N+1)P_N(\xi^N_i)}\frac{(1-\xi^2)P'_N(\xi)}{\xi^N_i - \xi}, & 0 < i < N, \\ \frac{(1+\xi)P'_N(\xi)}{N(N+1)}, & i = N. \end{cases} \tag{A19}$$

Note also that $l^N_i(\xi_j) = \delta_{ij}$, which is an important property inasmuch as it gives rise to the diagonality of the mass matrix. Derivatives $\partial_\xi\, l^N_i(\xi)$ are found using eq. (A14), as (Fournier 2004)

$$\partial_\xi l_i(\xi_I) = \begin{cases} \frac{P_N(\xi_I)}{P_N(\xi_i)}\frac{1}{\xi_I - \xi_i} & i \neq I, \\ \frac{-N(N+1)}{4} & i = I = 0, \\ \frac{N(N+1)}{4} & i = I = N, \\ 0 & \text{otherwise.} \end{cases} \tag{A20}$$

All of the above holds true for polynomial representation in the η direction for all elements, and the ξ direction for non-axial elements.

A3 Gauss-Lobatto–Jacobi (0,1) quadrature

A detailed description of different quadrature rules can be found in Bernardi *et al.* (1999) and Karniadakis & Sherwin (1999, Appendix B), where our specific case of (0,1) is given by setting the integrand powers equal to $\alpha = 0$ and $\beta = 1$. The polynomial representation of the ξ direction within axial elements is constructed using a different set of polynomials, defined by

$$\bar{P}_N(\xi) = \frac{P_N(\xi) + P_{N+1}(\xi)}{1+\xi}, \tag{A21}$$

satisfying the differential equation

$$\partial_\xi \left((1+\xi^2)(1-\xi)\partial_\xi \bar{P}_N\right) = -N(N+2)(1+\xi)\bar{P}_N. \tag{A22}$$

These polynomials are orthogonal in $\mathbb{L}^2_1$:

$$\int_{-1}^{1} \bar{P}_{N_1}(\xi)\bar{P}_{N_2}(\xi)(1+\xi)\, d\xi = \begin{cases} 0 & (N_1 \neq N_2), \\ 2/(N_1+1) & (N_1 = N_2). \end{cases} \tag{A23}$$

With starting values $\bar{P}_0(\xi) = 1$ and $\bar{P}_1(\xi) = \frac{1}{2}(3\xi - 1)$, the induction formula for $N \geq 1$ reads

$$\bar{P}_{N+1}(\xi) = \left[\frac{2N+3}{N+2}\xi - \frac{1}{(2N+1)(N+2)}\right]\bar{P}_N(\xi) - \frac{N(N+2)}{(2N+1)(2N+3)}\bar{P}_{N-1}(\xi). \tag{A24}$$

Here, we define Gauss-Lobatto–Jabobi points $\bar{\xi}_i^N,\ 0 \leq i \leq N$ as the zeroes of $(1-\xi^2)\partial_\xi \bar{P}_N(\xi)$. Gauss-Lobatto–Jacobi (0,1) quadrature weights $\bar{\sigma}_i^N$ are

$$\bar{\sigma}_i^N = \frac{4}{N(N+2)\bar{P}_N^2(\bar{\xi}_i^N)} \quad \text{for } 1 \leq i \leq N \text{ and } \bar{\sigma}_0^N = \frac{8}{N(N+2)(N+1)^2}. \tag{A25}$$

The corresponding basis functions may then be computed as

$$\bar{l}_i^N(\xi) = \begin{cases} \frac{2(-1)^N(\xi-1)\partial_\xi \bar{P}_N(\xi)}{N(N+1)(N+2)} & i = 0, \\ \frac{1}{N(N+2)\bar{P}_N(\bar{\xi}_I^N)} \frac{(1-\xi^2)\partial_\xi \bar{P}_N(\xi)}{\bar{\xi}_i^N - \xi} & 0 < i < N, \\ \frac{(1+\xi)\partial_\xi \bar{P}_N(\xi)}{N(N+2)} & i = N. \end{cases} \tag{A26}$$

Again, derivatives $\partial_\xi \bar{l}_i^N(\xi)$ may be found using eq. (A22), leading to (Fournier 2004)

$$\partial_\xi \bar{l}_i(\bar{\xi}_I) = \begin{cases} \frac{-N(N+2)}{6} & i = I = 0, \\ \frac{2(-1)^N \bar{P}_N(\bar{\xi}_I)}{(1+\bar{\xi}_I)(N+1)} & i = 0,\ 1 \leq I \leq N-1, \\ \frac{(-1)^N}{N+1} & i = 0,\ I = N, \\ \frac{(-1)^{N+1}(N+1)}{2\bar{P}_N(\bar{\xi}_i)(1+\bar{\xi}_i)} & 1 \leq i \leq N-1,\ I = 0, \\ \frac{1}{\bar{\xi}_I - \bar{\xi}_i} \frac{\bar{P}_N(\bar{\xi}_I)}{\bar{P}_N(\bar{\xi}_i)} & 1 \leq i \leq N-1,\ 1 \leq I \leq N-1, i \neq I, \\ \frac{-1}{2(1+\bar{\xi}_i)} & 1 \leq i \leq N-1,\ I = i, \\ \frac{1}{\bar{P}_N(\bar{\xi}_I)(1-\bar{\xi}_i)} & 1 \leq i \leq N-1,\ I = N, \\ \frac{(-1)^{N+1}(N+1)}{4} & i = N,\ I = 0, \\ \frac{-\bar{P}_N(\bar{\xi}_I)}{(1-\bar{\xi}_I)} & i = N,\ 1 \leq I \leq N-1, \\ \frac{N(N+2)-1}{4} & i = N,\ I = N. \end{cases} \tag{A27}$$

APPENDIX B: STIFFNESS TERMS

In this section, we present the whole stiffness term as a tensorized system for monopole, dipole and quadrupole source types.

B1 Matrix notation, tensor products and recast stiffness system

In the interest of a succinct description, we revert to matrix/vector notation as defined in Table A1. Let us start by rewriting the non-axial expressions eqs (34)–(37) in terms of these matrix operations as

$$\mathbf{R}_1^\alpha = {}_\epsilon\mathbf{A} \odot \mathbf{u}_\alpha, \tag{B1}$$

$$\mathbf{R}_2^\alpha = {}_\epsilon\mathbf{B}_{\chi_\eta} \odot \left(\mathbf{D}_\xi^{\mathrm{T}} \otimes \mathbf{u}_\alpha\right) + {}_\epsilon\mathbf{B}_{\chi_\xi} \odot (\mathbf{u}_\alpha \otimes \mathbf{D}_\eta), \tag{B2}$$

$$\mathbf{R}_3^\alpha = \mathbf{D}_\xi \otimes \left({}_\epsilon\mathbf{B}_{\chi_\eta} \odot \mathbf{u}_\alpha\right) + \left({}_\epsilon\mathbf{B}_{\chi_\xi} \odot \mathbf{u}_\alpha\right) \otimes \mathbf{D}_\eta^{\mathrm{T}}, \tag{B3}$$

Table A2. Pre-computed matrices $(E^{(k)}_{\beta\alpha})^{ij}$ of the leading order terms.

α	$k=1$	$k=2$	$k=3$	$k=4$
		Monopole & Quadrupole $\beta = s$		
s	$(\lambda^{ij}+2\mu^{ij})z_\xi^{ij}\,z_\eta^{ij}+\mu^{ij}\,s_\xi^{ij}\,s_\eta^{ij}$	$(\lambda^{ij}+2\mu^{ij})(z_\eta^{ij})^2+\mu^{ij}\,(s_\eta^{ij})^2$	$(\lambda^{ij}+2\mu^{ij})z_\xi^{ij}\,z_\eta^{ij}+\mu^{ij}\,s_\xi^{ij}\,s_\eta^{ij}$	$(\lambda^{ij}+2\mu^{ij})(z_\xi^{ij})^2+\mu^{ij}\,(s_\xi^{ij})^2$
z	$\lambda^{ij}\,s_\xi^{ij}\,z_\eta^{ij}+\mu^{ij}\,z_\xi^{ij}\,s_\eta^{ij}$	$(\lambda^{ij}+\mu^{ij})s_\eta^{ij}\,z_\eta^{ij}$	$\lambda^{ij}\,z_\xi^{ij}\,s_\eta^{ij}+\mu^{ij}\,s_\xi^{ij}\,z_\eta^{ij}$	$(\lambda^{ij}+\mu^{ij})s_\xi^{ij}\,z_\xi^{ij}$
		Monopole & Quadrupole $\beta = z$		
s	$\mu^{ij}\,z_\xi^{ij}\,z_\eta^{ij}+(\lambda^{ij}+2\mu^{ij})s_\xi^{ij}\,s_\eta^{ij}$	$\mu^{ij}\,(z_\eta^{ij})^2+(\lambda^{ij}+2\mu^{ij})(s_\eta^{ij})^2$	$\mu^{ij}\,z_\xi^{ij}\,z_\eta^{ij}+(\lambda^{ij}+2\mu^{ij})s_\xi^{ij}\,s_\eta^{ij}$	$\mu^{ij}\,(z_\xi^{ij})^2+(\lambda^{ij}+2\mu^{ij})(s_\xi^{ij})^2$
z	$\lambda^{ij}\,z_\xi^{ij}\,s_\eta^{ij}+\mu^{ij}\,s_\xi^{ij}\,z_\eta^{ij}$	$(\lambda^{ij}+\mu^{ij})s_\eta^{ij}\,z_\eta^{ij}$	$\lambda^{ij}\,s_\xi^{ij}\,z_\eta^{ij}+\mu^{ij}\,z_\xi^{ij}\,s_\eta^{ij}$	$(\lambda^{ij}+\mu^{ij})s_\xi^{ij}\,z_\xi^{ij}$
		Quadrupole $\beta = \phi$		
ϕ	$\mu^{ij}\,(z_\xi^{ij}\,z_\eta^{ij}+s_\xi^{ij}\,s_\eta^{ij})$	$\mu^{ij}\,((z_\eta^{ij})^2+(s_\eta^{ij})^2)$	$\mu^{ij}\,(z_\xi^{ij}\,z_\eta^{ij}+s_\xi^{ij}\,s_\eta^{ij})$	$\mu^{ij}\,((z_\xi^{ij})^2+(s_\xi^{ij})^2)$
		Dipole $\beta = +$		
$+$	$(\lambda^{ij}+3\mu^{ij})z_\xi^{ij}\,z_\eta^{ij}+2\mu^{ij}\,s_\xi^{ij}\,s_\eta^{ij}$	$(\lambda^{ij}+3\mu^{ij})(z_\eta^{ij})^2+2\mu^{ij}\,(s_\eta^{ij})^2$	$(\lambda^{ij}+3\mu^{ij})z_\xi^{ij}\,z_\eta^{ij}+2\mu^{ij}\,s_\xi^{ij}\,s_\eta^{ij}$	$(\lambda^{ij}+3\mu^{ij})(z_\xi^{ij})^2+2\mu^{ij}\,(s_\xi^{ij})^2$
$-$	$(\lambda^{ij}+\mu^{ij})z_\xi^{ij}\,z_\eta^{ij}$	$(\lambda^{ij}+\mu^{ij})(z_\eta^{ij})^2$	$(\lambda^{ij}+\mu^{ij})z_\xi^{ij}\,z_\eta^{ij}$	$(\lambda^{ij}+\mu^{ij})(z_\xi^{ij})^2$
z	$\lambda^{ij}\,s_\xi^{ij}\,z_\eta^{ij}+\mu^{ij}\,z_\xi^{ij}\,s_\eta^{ij}$	$(\lambda^{ij}+\mu^{ij})s_\eta^{ij}\,z_\eta^{ij}$	$\lambda^{ij}\,z_\xi^{ij}\,s_\eta^{ij}+\mu^{ij}\,s_\xi^{ij}\,z_\eta^{ij}$	$(\lambda^{ij}+\mu^{ij})s_\xi^{ij}\,z_\xi^{ij}$
		Dipole $\beta = -$		
$+$	$(\lambda^{ij}+\mu^{ij})z_\xi^{ij}\,z_\eta^{ij}$	$(\lambda^{ij}+\mu^{ij})(z_\eta^{ij})^2$	$(\lambda^{ij}+\mu^{ij})z_\xi^{ij}\,z_\eta^{ij}$	$(\lambda^{ij}+\mu^{ij})(z_\xi^{ij})^2$
$-$	$(\lambda^{ij}+3\mu^{ij})z_\xi^{ij}\,z_\eta^{ij}+2\mu^{ij}\,s^{ij}{}_\xi\,s^{ij}_\eta$	$(\lambda^{ij}+3\mu^{ij})(z_\eta^{ij})^2+2\mu^{ij}\,(s_\eta^{ij})^2$	$(\lambda^{ij}+3\mu^{ij})z_\xi^{ij}\,z_\eta^{ij}+2\mu^{ij}\,s_\xi^{ij}\,s_\eta^{ij}$	$(\lambda^{ij}+3\mu^{ij})(z_\xi^{ij})^2+2\mu^{ij}\,(s_\xi^{ij})^2$
z	$\lambda^{ij}\,s_\xi^{ij}\,z_\eta^{ij}+\mu^{ij}\,z_\xi^{ij}\,s_\eta^{ij}$	$(\lambda^{ij}+\mu^{ij})s_\eta^{ij}\,z_\eta^{ij}$	$\lambda^{ij}\,z_\xi^{ij}\,s_\eta^{ij}+\mu^{ij}\,s_\xi^{ij}\,z_\eta^{ij}$	$(\lambda^{ij}+\mu^{ij})s_\xi^{ij}\,z_\xi^{ij}$
		Dipole $\beta = z$		
$\pm$	$\lambda^{ij}\,z_\xi^{ij}\,s_\eta^{ij}+\mu^{ij}\,s_\xi^{ij}\,z_\eta^{ij}$	$(\lambda^{ij}+\mu^{ij})s_\eta^{ij}\,z_\eta^{ij}$	$\lambda^{ij}\,s_\xi^{ij}\,z_\eta^{ij}+\mu^{ij}\,z_\xi^{ij}\,s_\eta^{ij}$	$(\lambda^{ij}+\mu^{ij})s_\xi^{ij}\,z_\xi^{ij}$
z	$\mu^{ij}\,z_\xi^{ij}\,z_\eta^{ij}+(\lambda^{ij}+2\mu^{ij})s_\xi^{ij}\,s_\eta^{ij}$	$\mu^{ij}\,(z_\eta^{ij})^2+(\lambda^{ij}+2\mu^{ij})(s_\eta^{ij})^2$	$\mu^{ij}\,z_\xi^{ij}\,z_\eta^{ij}+(\lambda^{ij}+2\mu^{ij})s_\xi^{ij}\,s_\eta^{ij}$	$\mu^{ij}\,(z_\xi^{ij})^2+(\lambda^{ij}+2\mu^{ij})(s_\xi^{ij})^2$

$$\begin{aligned}\mathbf{R}_4^\alpha = {}& \mathbf{D}_\xi \otimes \left[\mathbf{C}\odot\mathbf{G}_1^{xy}\odot\left(\mathbf{u}_\alpha\otimes\mathbf{D}_\eta\right)\right]+\mathbf{D}_\xi\otimes\left[\mathbf{C}\odot\mathbf{G}_2^{xy}\odot\left(\mathbf{D}_\xi^{\mathrm{T}}\otimes\mathbf{u}_\alpha\right)\right]\\ &+\left[\mathbf{C}\odot\mathbf{G}_2^{xy}\odot\left(\mathbf{D}_\xi^{\mathrm{T}}\otimes\mathbf{u}_\alpha\right)\right]\otimes\mathbf{D}_\eta^{\mathrm{T}}+\left[\mathbf{C}\odot\mathbf{G}_3^{xy}\odot\left(\mathbf{u}_\alpha\otimes\mathbf{D}_\eta\right)\right]\otimes\mathbf{D}_\eta^{\mathrm{T}}.\end{aligned} \tag{B4}$$

The axial discretization eqs (38)–(41) takes the form

$$\bar{\mathbf{R}}_1^\alpha = \mathbf{R}_1^\alpha+\mathbf{D}_\xi^0\left[{}_\epsilon\mathbf{A}_0\odot\left((\mathbf{D}_\xi^0)^{\mathrm{T}}\otimes\mathbf{u}_\alpha\right)\right], \tag{B5}$$

$$\bar{\mathbf{R}}_2^\alpha = \mathbf{R}_2^\alpha+\left\{\begin{array}{ll}\mathbf{D}_\xi^0\left[{}_\epsilon\mathbf{A}_0\odot\left((\mathbf{D}_\xi^0)^{\mathrm{T}}\otimes\mathbf{u}_\alpha\right)\right] & (\partial_x=\partial_s)\\ \mathbf{D}_\xi^0\left[{}_\epsilon\mathbf{B}^0_{s_\xi}\odot\left(\mathbf{u}_\alpha^0\otimes\mathbf{D}_\eta\right)\right]+{}_\epsilon\mathbf{B}^0_{s_\xi}\odot\left[\left((\mathbf{D}_\xi^0)^{\mathrm{T}}\otimes\mathbf{u}_\alpha\right)\otimes\mathbf{D}_\eta\right] & (\partial_x=\partial_z)\end{array}\right\}, \tag{B6}$$

$$\bar{\mathbf{R}}_3^\alpha = \mathbf{R}_3^\alpha+\left\{\begin{array}{ll}\mathbf{D}_\xi^0\left[{}_\epsilon\mathbf{A}_0\odot\left((\mathbf{D}_\xi^0)^{\mathrm{T}}\otimes\mathbf{u}_\alpha\right)\right] & (\partial_x=\partial_s)\\ \mathbf{D}_\xi^0\left[\left({}_\epsilon\mathbf{B}^0_{s_\xi}\odot\mathbf{u}_\alpha^0\right)\otimes\mathbf{D}_\eta^{\mathrm{T}}\right]+\left[{}_\epsilon\mathbf{B}^0_{s_\xi}\odot\left((\mathbf{D}_\xi^0)^{\mathrm{T}}\otimes\mathbf{u}_\alpha\right)\right]\otimes\mathbf{D}_\eta^{\mathrm{T}} & (\partial_x=\partial_z)\end{array}\right\}, \tag{B7}$$

$$\bar{\mathbf{R}}_4^\alpha = \mathbf{R}_4^\alpha. \tag{B8}$$

We assumed here that whenever summation starts at $I>0$ as in eqs (38)–(40), then pre-computed matrices vanish at $I=0$. Both elemental operations $\otimes$ and $\odot$ are optimized using unrolled loops and unit-stride cache access (Deville *et al.* 2002). Schematically, we start out by computing all necessary $\otimes$ and $\odot$ operations, and then successively add different terms before computing the next round of operations $\otimes$ or $\odot$. For notational clarity, let $S=\sum_\beta S_\beta$, $\beta=s,\phi,z$ or $\beta=+,-,z$ be the original, continuous elemental stiffness integral such that $S\approx\mathbf{w}^{\mathrm{T}}\mathbf{K}\mathbf{u}$. We are then interested in evaluating the 'components' $(\mathbf{K}\mathbf{u})_\beta$. Additionally, we rearrange the integrand into the two sets $S_\beta=S_\beta^{\partial\partial}+S_\beta^{\partial}$ and accordingly, $(\mathbf{K}\mathbf{u})_\beta=(\mathbf{K}\mathbf{u})_\beta^{\partial\partial}+(\mathbf{K}\mathbf{u})_\beta^{\partial}$, where $S_\beta^{\partial\partial}$ is the collection of integrands containing derivatives of both w_β and u_α ('leading order'), and S_β^{∂} is the remaining part with maximally one derivative ('lower order').

B2 Leading order terms

For completeness, the analytical, initial integral form of the leading order terms is, for the monopole

$$S_s^{\partial\partial}=\int_{\Omega_e}\left[(\lambda+2\mu)\,\partial_s w_s\partial_s u_s+\lambda\partial_s w_s\partial_z u_z+\mu\partial_z w_s\,(\partial_s u_z+\partial_z u_s)\right]s\,ds\,dz, \tag{B9}$$

$$S_z^{\partial\partial} = \int_{\Omega_e} \left[(\lambda + 2\mu)\, \partial_z w_z \partial_z u_z + \lambda \partial_z w_z \partial_s u_s + \mu \partial_s w_z \left(\partial_s u_z + \partial_z u_s\right) \right] s\, ds\, dz, \tag{B10}$$

and for the dipole,

$$S_+^{\partial\partial} = \int_{\Omega_e} \left[(\lambda + 3\mu)\, \partial_s w_+ \partial_s u_+ + (\lambda + \mu)\, \partial_s w_+ \partial_s u_- + 2\mu \partial_z w_+ \partial_z u_+ + \lambda \partial_s w_+ \partial_z u_z + \mu \partial_z w_+ \partial_s u_z \right] s\, ds\, dz, \tag{B11}$$

$$S_-^{\partial\partial} = \int_{\Omega_e} \left[(\lambda + 3\mu)\, \partial_s w_- \partial_s u_- + (\lambda + \mu)\, \partial_s w_- \partial_s u_+ + 2\mu \partial_z w_- \partial_z u_- + \lambda \partial_s w_- \partial_z u_z + \mu \partial_z w_- \partial_s u_z \right] s\, ds\, dz, \tag{B12}$$

$$S_z^{\partial\partial} = \int_{\Omega_e} \left[\partial_z w_z \left[(\lambda + 2\mu)\, \partial_z u_z + \lambda \left(\partial_s u_+ + \partial_s u_-\right) \right] + \mu \partial_s w_z \left(\partial_s u_z + \partial_z u_+ + \partial_z u_-\right) \right] s\, ds\, dz. \tag{B13}$$

In the quadrupole case, $S_s^{\partial\partial}$ and $S_z^{\partial\partial}$ are identical to the monopole case, and we get additionally

$$S_\phi^{\partial\partial} = \int_{\Omega_e} \left[\partial_s w_\phi \partial_s u_\phi + \partial_z w_\phi \partial_z u_\phi \right] s\, ds\, dz. \tag{B14}$$

Rearranging these terms into groups of identical or partly similar operations, we end up with a system of pre-computed matrices detailed in Table A2 for the terms of the $\mathbf{R}_4^\alpha$-type and each source type. For any given element, this entire leading order part of the stiffness matrix is then compacted into

$$\begin{aligned}(\mathbf{Ku})_\beta^{\partial\partial} = \sum_\alpha \Big\{ &\mathbf{D}_\xi \otimes \left[\mathbf{C} \odot \mathbf{E}_{\beta\alpha}^{(1)} \odot (\mathbf{u}_\alpha \otimes \mathbf{D}_\eta) \right] + \mathbf{D}_\xi \otimes \left[\mathbf{C} \odot \mathbf{E}_{\beta\alpha}^{(2)} \odot (\mathbf{D}_\eta^{\mathrm{T}} \otimes \mathbf{u}_\alpha) \right] \\ &+ \left[\mathbf{C} \odot \mathbf{E}_{\beta\alpha}^{(3)} \odot \left(\mathbf{D}_\eta^{\mathrm{T}} \otimes \mathbf{u}_\alpha\right) \right] \otimes \mathbf{D}_\xi^{\mathrm{T}} + \left[\mathbf{C} \odot \mathbf{E}_{\beta\alpha}^{(4)} \odot \left(\mathbf{u}_\alpha \otimes \mathbf{D}_\eta\right) \right] \otimes \mathbf{D}_\xi^{\mathrm{T}} \Big\},\end{aligned} \tag{B15}$$

where the difference between source types is concentrated in $\mathbf{E}_{\beta\alpha}^{(k)}$. The quantities $\mathbf{E}_{\beta\alpha}^{(k)}$ are listed in Table A2 for monopole, dipole, and quadrupole source types, respectively. The difference in axial versus non-axial elements is abundant in quantities **C** and **D** as defined in Table 1. The explicit expansion of all lower-order terms for axial or non-axial elements is given in the following subsections for each source type separately.

B3 Lower-order terms: Monopole

The lower-order terms for the monopole case are

$$S_s^\partial = \int_{\Omega_e} \left\{ (\lambda + 2\mu)\, \frac{w_s u_s}{s^2} + \lambda \left[\partial_s w_s \frac{u_s}{s} + \frac{w_s}{s} \left(\partial_s u_s + \partial_z u_z\right) \right] \right\} s\, ds\, dz, \tag{B16}$$

$$S_z^\partial = \int_{\Omega_e} \lambda \partial_z w_z \frac{u_s}{s} s\, ds\, dz. \tag{B17}$$

Honouring the additional terms exclusive to axial elements (see eqs B5–B7), we will develop the discretization with these additional terms in curly braces being preceded by $\delta_{e\bar{e}}$, such that the description applies to all elements. The discretized form for any element unfolds as

$$\begin{aligned}(\mathbf{Ku})_s^\partial = {}& {}_\lambda\mathbf{B}_{s_\xi} \odot \left(\mathbf{u}_z \otimes \mathbf{D}_\eta\right) + {}_\lambda\mathbf{B}_{s_\eta} \odot \left(\mathbf{D}_\xi^{\mathrm{T}} \otimes \mathbf{u}_z\right) + {}_\lambda\mathbf{B}_{z_\xi} \odot \left(\mathbf{u}_s \otimes \mathbf{D}_\eta\right) + {}_\lambda\mathbf{B}_{z_\eta} \odot \left(\mathbf{D}_\xi^{\mathrm{T}} \otimes \mathbf{u}_s\right) + \mathbf{D}_\xi \otimes \left({}_\lambda\mathbf{B}_{z_\eta} \odot \mathbf{u}_s\right) \\ &+ \left({}_\lambda\mathbf{B}_{z_\xi} \odot \mathbf{u}_s\right) \otimes \mathbf{D}_\eta^{\mathrm{T}} + {}_{(\lambda+2\mu)}\mathbf{A} \odot \mathbf{u}_s + \delta_{e\bar{e}} \left\{ \mathbf{D}_\xi^0 \left[{}_\lambda\mathbf{B}_{s_\xi}^0 \odot \left(\mathbf{u}_z^0 \otimes \mathbf{D}_\eta\right) + {}_{3\lambda+2\mu}\mathbf{A}_0 \odot \left(\left(\mathbf{D}_\xi^0\right)^T \otimes \mathbf{u}_s \right) \right] \right\},\end{aligned} \tag{B18}$$

$$(\mathbf{Ku})_z^\partial = \mathbf{D}_\xi \otimes \left({}_\lambda\mathbf{B}_{s_\eta} \odot \mathbf{u}_s\right) + \left({}_\lambda\mathbf{B}_{s_\xi} \odot \mathbf{u}_s\right) \otimes \mathbf{D}_\eta^{\mathrm{T}} + \delta_{e\bar{e}} \left\{ \left[{}_\lambda\mathbf{B}_{s_\xi}^0 \odot \left(\left(\mathbf{D}_\xi^0\right)^{\mathrm{T}} \otimes \mathbf{u}_s \right) \right] \otimes \mathbf{D}_\eta^{\mathrm{T}} \right\}. \tag{B19}$$

B4 Lower-order terms: Dipole

We again write the dipole system in the $(+, -, z)$ coordinate system to properly implement the axial boundary conditions in eq. (4). After rearrangement, the stiffness system of lower-order terms then takes the form

$$S_+^\partial = \int_{\Omega_e} \left\{ 2\left(\lambda + \mu\right) \partial_s w_+ \frac{u_-}{s} + \mu \partial_z w_+ \frac{u_z}{s} \right\} s\, ds\, dz, \tag{B20}$$

$$S_-^\partial = \int_{\Omega_e} \left\{ 2\left(\lambda - \mu\right) \partial_s w_- \frac{u_-}{s} - \mu \partial_z w_- \frac{u_z}{s} + 2\frac{w_-}{s} \left[2\left(\lambda + 3\mu\right) \frac{u_-}{s} + \left(\lambda + \mu\right) \partial_s u_+ + \left(\lambda - \mu\right) \partial_s u_- + \lambda \partial_z u_z \right] \right\} s\, ds\, dz, \tag{B21}$$

$$S_z^\partial = \int_{\Omega_e} \left\{ 2\lambda \partial_z w_z \frac{u_-}{s} + \mu \frac{w_z}{s} \left(\partial_z u_+ - \partial_z u_- + \frac{u_z}{s} \right) \right\} s\, ds\, dz. \tag{B22}$$

For any element, the discretized version of the lower-order terms of the dipole stiffness term is

$$(\mathbf{Ku})^{\partial}_{+} = \mathbf{D}_\xi \otimes \left({}_{2(\lambda+\mu)}\mathbf{B}_{z_\eta} \odot \mathbf{u}_-\right) + \left({}_{2(\lambda+\mu)}\mathbf{B}_{z_\xi} \odot \mathbf{u}_-\right) \otimes \mathbf{D}_\eta^{\mathrm{T}} + \mathbf{D}_\xi \otimes \left({}_{\mu}\mathbf{B}_{s_\eta} \odot \mathbf{u}_z\right) + \left({}_{\mu}\mathbf{B}_{s_\xi} \odot \mathbf{u}_z\right) \otimes \mathbf{D}_\eta^{\mathrm{T}}$$
$$+\delta_{e\bar{e}}\left\{\mathbf{D}_\xi^0\left[{}_{2(\lambda+\mu)}\mathbf{A}_0 \odot \left(\left(\mathbf{D}_\xi^0\right)^{\mathrm{T}} \otimes \mathbf{u}_-\right)\right] + \left[{}_{\mu}\mathbf{B}^0_{s_\xi} \odot \left(\left(\mathbf{D}_\xi^0\right)^{\mathrm{T}} \otimes \mathbf{u}_z\right)\right] \otimes \mathbf{D}_\eta^{\mathrm{T}}\right\}, \tag{B23}$$

$$(\mathbf{Ku})^{\partial}_{-} = \mathbf{D}_\xi \otimes \left({}_{2(\lambda-\mu)}\mathbf{B}_{z_\eta} \odot \mathbf{u}_-\right) + \left({}_{2(\lambda-\mu)}\mathbf{B}_{z_\xi} \odot \mathbf{u}_-\right) \otimes \mathbf{D}_\eta^{\mathrm{T}} - \mathbf{D}_\xi \otimes \left({}_{\mu}\mathbf{B}_{s_\eta} \odot \mathbf{u}_z\right) - \left({}_{\mu}\mathbf{B}_{s_\xi} \odot \mathbf{u}_z\right) \otimes \mathbf{D}_\eta^{\mathrm{T}}$$
$$+{}_{4(\lambda+3\mu)}\mathbf{A} \odot \mathbf{u}_- + 2{}_{\lambda}\mathbf{B}_{s_\xi} \odot \left(\mathbf{u}_z \otimes \mathbf{D}_\eta\right) + 2{}_{\lambda}\mathbf{B}_{s_\eta} \odot \left(\mathbf{D}_\xi^{\mathrm{T}} \otimes \mathbf{u}_z\right) + {}_{2(\lambda+\mu)}\mathbf{B}_{z_\eta} \odot \left(\mathbf{D}_\xi^{\mathrm{T}} \otimes \mathbf{u}_+\right)$$
$$+{}_{2(\lambda-\mu)}\mathbf{B}_{z_\eta} \odot \left(\mathbf{D}_\xi^{\mathrm{T}} \otimes \mathbf{u}_-\right) + {}_{2(\lambda+\mu)}\mathbf{B}_{z_\xi} \odot \left(\mathbf{u}_+ \otimes \mathbf{D}_\eta\right) + {}_{2(\lambda-\mu)}\mathbf{B}_{z_\xi} \odot \left(\mathbf{u}_- \otimes \mathbf{D}_\eta\right)$$
$$+\delta_{e\bar{e}}\left\{\mathbf{D}_\xi^0\left[{}_{2(\lambda+\mu)}\mathbf{A}_0 \odot \left(4\left(\mathbf{D}_\xi^0\right)^{\mathrm{T}} \otimes \mathbf{u}_- + \left(\mathbf{D}_\xi^0\right)^{\mathrm{T}} \otimes \mathbf{u}_+\right)\right]\right\}, \tag{B24}$$

$$(\mathbf{Ku})^{\partial}_{z} = \mathbf{D}_\xi \otimes \left({}_{2\lambda}\mathbf{B}_{s_\eta} \odot \mathbf{u}_-\right) + \left({}_{2\lambda}\mathbf{B}_{s_\xi} \odot \mathbf{u}_-\right) \otimes \mathbf{D}_\eta^{\mathrm{T}} + {}_{\mu}\mathbf{A} \odot \mathbf{u}_z + {}_{\mu}\mathbf{B}_{s_\xi} \odot \left[\left(\mathbf{u}_+ - \mathbf{u}_-\right) \otimes \mathbf{D}_\eta\right]$$
$$+{}_{\mu}\mathbf{B}_{s_\eta} \odot \left[\mathbf{D}_\xi^{\mathrm{T}} \otimes \left(\mathbf{u}_+ - \mathbf{u}_-\right)\right] + \delta_{e\bar{e}}\left\{\mathbf{D}_\xi^0\left[{}_{\mu}\mathbf{A}_0 \odot \left(\left(\mathbf{D}_\xi^0\right)^{\mathrm{T}} \otimes \mathbf{u}_z\right) + {}_{\mu}\mathbf{B}^0_{s_\xi} \odot \left(\mathbf{u}^0_+ \otimes \mathbf{D}_\eta\right)\right]\right\}. \tag{B25}$$

This system is computationally slightly more expensive than the monopole case.

B5 Lower-order terms: Quadrupole

In the quadrupole case, lower-order terms of the integral form eq. (7) are

$$S_s^{\partial} = \int_{\Omega_e}\left\{(\lambda+2\mu)\frac{w_s}{s^2}\left(u_s - 2u_\phi\right) + \lambda\left[\partial_s w_s \frac{u_s - 2u_\phi}{s} + \frac{w_s}{s}\left(\partial_s u_s + \partial_z u_z\right)\right] + 2\mu\frac{w_s}{s}\left(\partial_s u_\phi + \frac{2u_s - u_\phi}{s}\right)\right\} s\, ds\, dz, \tag{B26}$$

$$S_\phi^{\partial} = \int_{\Omega_e}\left\{\frac{w_\phi}{s}\left[-(2\lambda+6\mu)\frac{u_s}{s} + (4\lambda+9\mu)\frac{u_\phi}{s} - \lambda\partial_s u_s + \lambda\partial_z u_z - \mu\partial_s u_\phi\right] + \mu\partial_s w_\phi\frac{2u_s - u_\phi}{s} + 2\mu\partial_z w_\phi\frac{u_z}{s}\right\} s\, ds\, dz, \tag{B27}$$

$$S_z^{\partial} = \int_{\Omega_e}\left\{\lambda\partial_z w_z\frac{u_s - 2u_\phi}{s} + 2\mu\frac{w_z}{s}\left(\partial_z u_\phi + \frac{2u_z}{s}\right)\right\} s\, ds\, dz. \tag{B28}$$

The discretized version for the lower-order terms in the quadrupole case reads

$$(\mathbf{Ku})^{\partial}_{s} = {}_{\lambda}\mathbf{B}_{s_\xi} \odot \left(\mathbf{u}_z \otimes \mathbf{D}_\eta\right) + {}_{\lambda}\mathbf{B}_{s_\eta} \odot \left(\mathbf{D}_\xi^{\mathrm{T}} \otimes \mathbf{u}_z\right) + {}_{\lambda}\mathbf{B}_{z_\xi} \odot \left(\mathbf{u}_s \otimes \mathbf{D}_\eta\right) + {}_{\lambda}\mathbf{B}_{z_\eta} \odot \left(\mathbf{D}_\xi^{\mathrm{T}} \otimes \mathbf{u}_s\right)$$
$$+\mathbf{D}_\xi \otimes \left({}_{\lambda}\mathbf{B}_{z_\eta} \odot \mathbf{u}_s\right) + \left({}_{\lambda}\mathbf{B}_{z_\xi} \odot \mathbf{u}_s\right) \otimes \mathbf{D}_\eta^{\mathrm{T}} + {}_{(\lambda+6\mu)}\mathbf{A} \odot \mathbf{u}_s - \mathbf{D}_\xi \otimes \left({}_{2\lambda}\mathbf{B}_{z_\eta} \odot \mathbf{u}_\phi\right)$$
$$-\left({}_{2\lambda}\mathbf{B}_{z_\xi} \odot \mathbf{u}_\phi\right) \otimes \mathbf{D}_\eta^{\mathrm{T}} + {}_{2\mu}\mathbf{B}_{z_\xi} \odot \left(\mathbf{u}_\phi \otimes \mathbf{D}_\eta\right) + {}_{2\mu}\mathbf{B}_{z_\eta} \odot \left(\mathbf{D}_\xi^{\mathrm{T}} \otimes \mathbf{u}_\phi\right) - {}_{2\lambda+6\mu}\mathbf{A} \odot \mathbf{u}_\phi$$
$$+\delta_{e\bar{e}}\left\{\mathbf{D}_\xi^0\left[{}_{3(\lambda+2\mu)}\mathbf{A}_0 \odot \left(\left(\mathbf{D}_\xi^0\right)^{\mathrm{T}} \otimes \mathbf{u}_s\right) - {}_{4(\lambda+\mu)}\mathbf{A}_0 \odot \left(\left(\mathbf{D}_\xi^0\right)^{\mathrm{T}} \otimes \mathbf{u}_\phi\right)\right]\right\}, \tag{B29}$$

$$(\mathbf{Ku})^{\partial}_{\phi} = \mathbf{D}_\xi \otimes \left({}_{2\mu}\mathbf{B}_{z_\eta} \odot \mathbf{u}_s\right) + \left({}_{2\mu}\mathbf{B}_{z_\xi} \odot \mathbf{u}_s\right) \otimes \mathbf{D}_\eta^{\mathrm{T}} - \mathbf{D}_\xi \otimes \left({}_{\mu}\mathbf{B}_{z_\eta} \odot \mathbf{u}_\phi\right) - \left({}_{\mu}\mathbf{B}_{z_\xi} \odot \mathbf{u}_\phi\right) \otimes \mathbf{D}_\eta^{\mathrm{T}} + \mathbf{D}_\xi \otimes \left({}_{2\mu}\mathbf{B}_{s_\eta} \odot \mathbf{u}_z\right)$$
$$+\left({}_{2\mu}\mathbf{B}_{s_\xi} \odot \mathbf{u}_z\right) \otimes \mathbf{D}_\eta^{\mathrm{T}} - 2{}_{\lambda}\mathbf{B}_{z_\xi} \odot \left(\mathbf{u}_s \otimes \mathbf{D}_\eta\right) - 2{}_{\lambda}\mathbf{B}_{z_\eta} \odot \left(\mathbf{D}_\xi^{\mathrm{T}} \otimes \mathbf{u}_s\right) - 2{}_{\lambda}\mathbf{B}_{s_\xi} \odot \left(\mathbf{u}_z \otimes \mathbf{D}_\eta\right)$$
$$-2{}_{\lambda}\mathbf{B}_{s_\eta} \odot \left(\mathbf{D}_\xi^{\mathrm{T}} \otimes \mathbf{u}_z\right) - {}_{\mu}\mathbf{B}_{z_\xi} \odot \left(\mathbf{u}_\phi \otimes \mathbf{D}_\eta\right) + {}_{\mu}\mathbf{B}_{z_\eta} \odot \left(\mathbf{D}_\xi^{\mathrm{T}} \otimes \mathbf{u}_\phi\right) - {}_{2\lambda+6\mu}\mathbf{A} \odot \mathbf{u}_s + {}_{4\lambda+9\mu}\mathbf{A} \odot \mathbf{u}_\phi$$
$$+\delta_{e\bar{e}}\left\{\mathbf{D}_\xi^0\left[-{}_{4(\lambda+\mu)}\mathbf{A}_0 \odot \left(\left(\mathbf{D}_\xi^0\right)^{\mathrm{T}} \otimes \mathbf{u}_s\right) + {}_{4\lambda+7\mu}\mathbf{A}_0 \odot \left(\left(\mathbf{D}_\xi^0\right)^{\mathrm{T}} \otimes \mathbf{u}_\phi\right)\right]\right\}, \tag{B30}$$

$$(\mathbf{Ku})^{\partial}_{z} = \mathbf{D}_\xi \otimes \left({}_{\lambda}\mathbf{B}_{s_\eta} \odot \mathbf{u}_s\right) + \left({}_{\lambda}\mathbf{B}_{s_\xi} \odot \mathbf{u}_s\right) \otimes \mathbf{D}_\eta^{\mathrm{T}} - \mathbf{D}_\xi \otimes \left({}_{2\lambda}\mathbf{B}_{s_\eta} \odot \mathbf{u}_\phi\right) - \left({}_{2\lambda}\mathbf{B}_{s_\xi} \odot \mathbf{u}_\phi\right) \otimes \mathbf{D}_\eta^{\mathrm{T}}$$
$$+{}_{2\mu}\mathbf{B}_{s_\xi} \odot \left(\mathbf{u}_\phi \otimes \mathbf{D}_\eta\right) + {}_{2\mu}\mathbf{B}_{s_\eta} \odot \left(\mathbf{D}_\xi^{\mathrm{T}} \otimes \mathbf{u}_\phi\right) + {}_{4\mu}\mathbf{A} \odot \mathbf{u}_z + \delta_{e\bar{e}}\left\{\mathbf{D}_\xi^0\left[{}_{4\mu}\mathbf{A}_0 \odot \left(\left(\mathbf{D}_\xi^0\right)^{\mathrm{T}} \otimes \mathbf{u}_z\right)\right]\right\}. \tag{B31}$$

Since all components vanish at the axis, all non-zero additional terms are of the same kind and for $\partial_x = \partial_s$. Note that the non-axial quadrupole case includes the non-axial monopole case.

APPENDIX C: TOROIDAL EIGENFUNCTIONS IN A HOMOGENEOUS SPHERE

In this section, we derive toroidal eigenfunctions for the dipole and quadrupole excitation types. These functions satisfy the source-free, frequency-domain wave equation

$$-\rho\omega^2\mathbf{u} = \boldsymbol{\nabla}\cdot\mathbf{T} \text{ in } \Omega, \tag{C1}$$

subject to the traction-free surface boundary condition $\hat{\mathbf{r}}\cdot\mathbf{T} = \mathbf{0}$ at $|\mathbf{r}| = r_0$. After multiplication with a test function and partial integration, the resultant weak form corresponding to eq. (C1) leads to the discretized, global linear system

$$\mathbf{Ku} = {}_{n}\omega_l^2\mathbf{Mu}, \tag{C2}$$

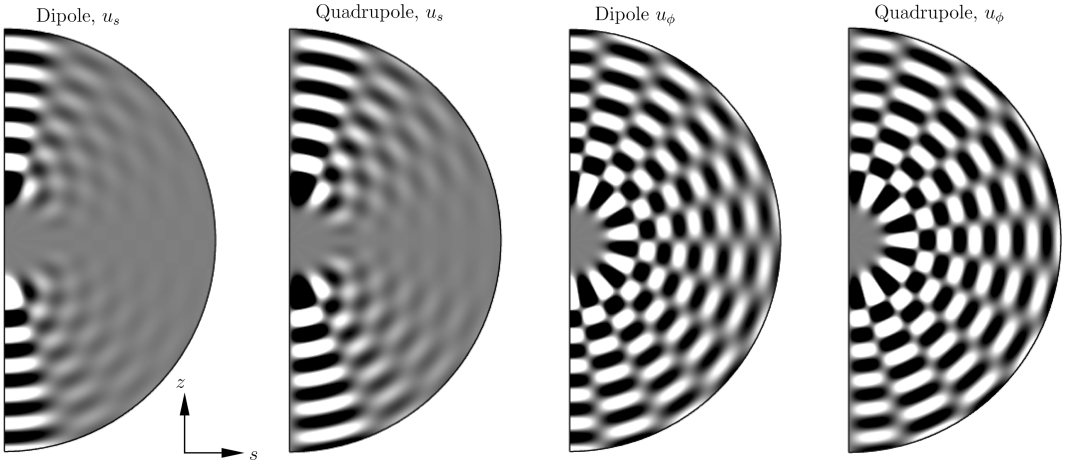

Figure A2. Toroidal eigenfunctions in a homogeneous sphere for $l = n = 11$. Shown are the s and ϕ components of the dipole eigenfunction $\mathbf{u}_1$ (eq. C7) and the quadrupole eigenfunction $\mathbf{u}_2$ (eq. C8), respectively as denoted above each plot. These functions multiplied with ${}_n\omega_l^2$ are the reference solution to be compared to the term $\mathbf{M}^{-1}(\mathbf{Ku})$ as obtained by the spectral-element approach of this paper. Shading is indicative of positive (white) and negative (black) displacements.

similar to eq. (18). Given a known solution $\mathbf{u}$ to eq. (C1), we proceed with eq. (C2) using the exact same approach as detailed in Section 4, setting $\mathbf{f} = \mathbf{0}$. A solution $\mathbf{u}$ is the toroidal eigenfunction, given by (Dahlen & Tromp 1998)

$$\mathbf{u}(\mathbf{r}) = j_l({}_n\omega_l r/v_s)\,[-\hat{\mathbf{r}} \times \boldsymbol{\nabla}_1 X_{lm}(\theta) \sin m\phi]\,, \tag{C3}$$

where j_l are spherical Bessel functions (Zhang & Jin 1996), ${}_n\omega_l$ are the toroidal eigenfrequencies of degree l and overtone n, v_s is the constant shear-wave velocity, $-\hat{\mathbf{r}} \times \boldsymbol{\nabla}_1 = -\hat{\boldsymbol{\phi}}\partial_\theta + \hat{\boldsymbol{\theta}}(\sin\theta)^{-1}\partial_\phi$, and X_{lm} are harmonics with order m. Ignoring normalization factors (i.e. $X_{lm} \rightarrow P_{lm}$), we obtain eigenfunctions for a given eigenfrequency ${}_n\omega_l$,

$$\mathbf{u}_m(\mathbf{r}) = j_l({}_n\omega_l r/v_s)\left[-\hat{\boldsymbol{\phi}}\partial_\theta P_{lm}(\cos\theta)\sin m\phi + \hat{\boldsymbol{\theta}}\tfrac{m}{\sin\theta} P_{lm}(\cos\theta)\cos m\phi\right] =$$

$$j_l({}_n\omega_l r/v_s)\left[(\hat{\mathbf{s}}\cot\theta - \hat{\mathbf{z}})\, m P_{lm}(\cos\theta)\cos m\phi - \hat{\boldsymbol{\phi}}\partial_\theta P_{lm}(\cos\theta)\sin m\phi\right], \tag{C4}$$

where P_{lm} are the associated Legendre functions

$$P_{lm}(\mu) = (1-\mu^2)^{m/2}\left(\frac{d}{d\mu}\right)^m P_l(\mu) \tag{C5}$$

with $\mu = \cos\theta$ and Legendre polynomials $P_l(\mu)$ as defined in eq. (A15). The derivatives $R_{lm}(\mu) = (\frac{d}{d\mu})^m P_l(\mu)$ may be computed using the recursion formula from (Dahlen & Tromp 1998, eq. B.115)

$$R_{l+1\,m}(\mu) = [(2l+1)\mu R_{lm}(\mu) - (l+m)R_{l-1\,m}(\mu)]\,(l-m+1)^{-1} \tag{C6}$$

with starting values $R_{11} = 1$, $R_{21} = 3\mu$, $R_{22} = 3$, and $R_{32} = 15\mu$. Using common identities for the derivatives of Legendre polynomials (Dahlen & Tromp 1998), we then find for the dipole case

$$\mathbf{u}_1(r,\theta,{}_n\omega_l) = j_l\left(\frac{{}_n\omega_l r}{v_s}\right)\left\{\hat{\mathbf{s}}R_{l1}(\cos\theta)\cos\theta + \hat{\boldsymbol{\phi}}\left[R_{l1}(\cos\theta)\cos\theta - R_{l2}(\cos\theta)\sin^2\theta\right] - \hat{\mathbf{z}}R_{l1}(\cos\theta)\sin\theta\right\}. \tag{C7}$$

Similarly, the eigenfunctions for the quadrupole case are

$$\mathbf{u}_2(r,\theta,{}_n\omega_l) = j_l\left(\frac{{}_n\omega_l r}{v_s}\right)\sin\theta\left\{\hat{\mathbf{s}}2R_{l2}(\cos\theta)\cos\theta + \hat{\boldsymbol{\phi}}\left[(l-1)(l+2)R_{l1}(\cos\theta) - 2R_{l2}(\cos\theta)\cos\theta\right] - \hat{\mathbf{z}}2R_{l2}(\cos\theta)\sin\theta\right\}. \tag{C8}$$

Note the multiplicative factor $\sin\theta$ which satisfies the axial boundary conditions eq. (4) for the quadrupole. Eqs (C8) and (C7) compose the system used for the SEM validation. Fig. A2 illustrates the s and ϕ components of $\mathbf{u}$ for dipole and quadrupole cases, respectively, at $l = n = 11$, where shading indicates positive (white) and negative (black) displacements. In the spherical coordinate system, we obtain for both dipole and quadrupole cases, after dropping dependencies, $\hat{\boldsymbol{\theta}} \cdot \mathbf{u}_m = j_l R_{lm}$, $\hat{\mathbf{r}} \cdot \mathbf{u}_m = 0$, and $\hat{\boldsymbol{\phi}} \cdot \mathbf{u}_m$ as in the cylindrical case. The eigenfrequencies ${}_n\omega_l$ are numerically computed by solving

$$(l-1)\,j_l\left(\frac{\omega r_0}{v_s}\right) = \left(\frac{\omega r_0}{v_s}\right) j_{l+1}\left(\frac{\omega r_0}{v_s}\right) \tag{C9}$$

for each l via standard root-finding. In summary, we insert eigenfunctions $\mathbf{u}$ into our SEM and compute $\mathbf{Ku}$ following Appendix B. The validation then lies in using the SEM to compute $\mathbf{M}^{-1}(\mathbf{Ku})$ and comparing the result with ${}_n\omega_1{}^2\mathrm{u}$.